The 2017 reversal of the Beaufort Gyre: Can dynamic thickening of a seasonal ice cover during a reversal limit summer ice melt in the Beaufort Sea?

Babb, D.G.[1] (david.babb@umanitoba.ca), J.C. Landy[2], J.V. Lukovich[1], C. Haas[3], S. Hendricks[3], D.G. Barber[1], R.J. Galley[1]

[1] Centre for Earth Observation Science, University of Manitoba, Winnipeg, MB, Canada

[2] Bristol Glaciology Centre, University of Bristol, Bristol, United Kingdom

[3] Alfred Wegener Institute Helmholtz-Center for Polar and Marine Research, Bremerhaven, Germany

Re-Submitted to JGR-Oceans (Paper #2020JC016796)

Key Points

1. The Beaufort Gyre reversal during winter 2017 drove anomalous sea ice convergence against the Canadian Arctic in the Beaufort Sea.
2. Deformation transformed an anomalously thin seasonal ice cover into the roughest and thickest end of winter ice pack in the CryoSat-2 record.
3. Despite being conditioned to limit summer melt, spring dynamics broke up the ice pack and led to another low ice year in the Beaufort Sea.

Abstract

During winter 2017 the semi-permanent Beaufort High collapsed and the anticyclonic Beaufort Gyre reversed. The reversal drove eastward ice motion through the Western Arctic, causing sea ice to converge against Banks Island, and halted the circulation of multiyear sea ice via the gyre, preventing its replenishment in the Beaufort Sea. Prior to the reversal, an anomalously thin seasonal ice cover had formed in the Beaufort following ice-free conditions during September 2016. With the onset of the reversal in January 2017, convergence drove uncharacteristic dynamic thickening during winter. By the end of March, despite seasonal ice comprising 97% of the ice cover, the reversal created the thickest, roughest and most voluminous regional ice cover of the CryoSat-2 record. Within the Beaufort Sea, previous work has shown that winter ice export can precondition the region for increased summer ice melt, but that a short reversal during April 2013 contributed to a reduction in summer ice loss. Hence the deformed ice cover at the end of winter 2017 could

be expected to limit summer melt. In spite of this, the Beaufort ice cover fell to its fourth lowest September area as the gyre re-established during April and divergent ice drift broke up the pack, negating the reversal's earlier preconditioning. Our work highlights that dynamic winter thickening of a regional sea ice cover, for instance during a gyre reversal, offers the potential to limit summer ice loss, but that dynamic forcing during spring dictates whether this conditioning carries through to the melt season.

Plain Language Summary:

The Beaufort Gyre is a semi-permanent feature that transports sea ice clockwise from the High Arctic through the Beaufort and Chukchi Seas. Occasionally the Gyre reverses, transporting sea ice counterclockwise. Historically these reversals only occurred during summer, but as the arctic changes reversals have become more frequent and more pronounced, and during winter 2017 the gyre underwent a prolonged reversal. Using a mix of satellite-based and in situ observations we examine how this reversal affected the ice cover of the Western Arctic. By altering the patterns of sea ice motion and forcing sea ice in the Beaufort Sea to converge against the coast, the reversal transformed the ice cover from an anomalously thin seasonal ice cover in fall to an anomalously thick and rough ice cover by the end of winter. Theoretically this conditioned the ice cover for limited summer ice loss. However this was not the case as the ice cover broke up prematurely during spring, allowing the sun to warm surface waters and melt the ice through the ice-albedo feedback. By September the ice cover fell to its fourth lowest regional minimum as the Beaufort ice cover continues to decline.

1. Introduction:

The anticyclonic Beaufort Gyre is one of the defining characteristics of the Arctic Ocean. The Gyre is driven by the semi-permanent Beaufort High (Serreze & Barrett, 2011), which circulates sea ice anticyclonically (Rigor & Wallace, 2002) and has been accumulating a large volume of freshwater in the western Arctic (Giles et al., 2012; Andrey Proshutinsky et al., 2009). Historically the gyre has occasionally reversed for short periods of time as cyclones passed through the region, causing cyclonic ice drift (Mclaren et al., 1987; Serreze et al., 1989) and allowing freshwater to be released from the gyre (Manucharyan & Spall, 2016; Meneghello et al., 2018). Generally these reversals have only occurred during summer, when the mechanically weak and therefore more mobile ice cover was more responsive to cyclones (LeDrew et al., 1991; Lukovich & Barber, 2006; Mclaren et al., 1987; Preller & Posey, 1989; Serreze et al., 1989). However, Lukovich and Barber (2006) found episodic reversals of the Beaufort Gyre throughout the annual cycle from 1979 to 2001, while Asplin et al., (2009) found that reversals in the Gyre have become more frequent throughout the year, which they attributed to the mechanical weakening of the Arctic ice cover. In recent years there have been two pronounced reversals of the Beaufort Gyre during winter. In 2013 an approximately two-week reversal occurred during April (Babb et al., 2019) due to a cyclone passing through the region. In 2017 a prolonged reversal occurred throughout winter because the Beaufort High collapsed and created an anomalous meridional pressure gradient over the western Arctic (Moore et al., 2018). The 2017 reversal has been attributed to cyclonic intrusions from the North Atlantic that were facilitated by negative sea ice anomalies in the Barents Sea (Moore et al., 2018). While the substantial duration of the 2017 reversal was unique within the observational record, Moore et al., (2018) suggest that as the Arctic ice cover continues to thin and decline in extent such reversals may become more common and exert a considerable impact on the physical and biogeochemical processes of the Arctic Ocean.

Reversals of the Beaufort Gyre are of particular interest because they alter the patterns of sea ice motion and therefore affect the dynamic properties and state of the ice cover, though the effect of reversals on the ice cover has never been studied in detail. Additionally, reversals facilitate the release of freshwater from the Gyre, which may have pronounced impacts on downstream areas such as the North Atlantic by increasing stratification and limiting deep water formation (Aagaard & Carmack, 1989; Curry & Mauritzen, 2005; Dickson et al., 1988; Giles et al., 2012). The anomalous atmospheric

meridional pressure gradient during the 2017 reversal drove eastward ice motion through the western Arctic, advecting sea ice against Banks Island (Moore et al., 2018). However, analysis of how this pronounced reversal affected the ice cover was limited to a brief interpretation of seasonal outputs from the PIOMAS ice-ocean model (Zhang & Rothrock, 2003), from which ice thickness anomalies in the Beaufort Sea were confounded by negative ice thickness anomalies throughout the entire Arctic Ocean as a result of long-term trends (1979 - 2017) towards thinner sea ice (Moore et al., 2018). Previous work on the impact of reversals on the state of the ice cover is limited, but within the Beaufort Sea there is scarce but dependable evidence that reversals deform the ice cover. For example, repeated reversals during winter 1993 were shown to dramatically increase *in situ* observations of ice draft over the Beaufort Sea shelf (Melling et al., 2005), while on a broader scale the transient reversal during April 2013 drove convergent ice drift against the western coast of the Canadian Arctic Archipelago (CAA) and substantially increased the regional ice volume (Babb et al., 2019). Following the 2013 event itself, the ice cover remained consolidated, which delayed spring breakup (Babb et al., 2019). High sea level pressure over the Beaufort during summer 2013 (Howell et al., 2016) maintained a compact ice cover throughout summer (Kwok, 2015), limiting regional summer ice loss and maintaining thicker ice into winter 2014 (Babb et al., 2019; Tilling et al., 2015). Under the typical anticyclonic pattern of the Beaufort Gyre, sea ice convergence and deformation occurs further north against the coast of the CAA and northern Greenland (Bourke & Garret, 1987; Kwok, 2015), but when the Gyre reverses sea ice instead converges farther south in the Beaufort Sea against the west coast of Banks Island. In 2013 convergence of the Beaufort ice cover against Banks Island during the reversal contributed to a recovery of the regional ice cover and gave credence to the idea that reversals may condition the ice cover for reduced summer melt.

The ice cover of the Beaufort Sea is a mix of first year sea ice (FYI) and multiyear sea ice (MYI), with the Beaufort Gyre typically importing MYI from the central Arctic and exporting a mix of FYI and MYI westward into the Chukchi Sea (Galley et al., 2013; Howell et al., 2016). New ice forms throughout winter within narrow leads within the pack ice and in an extensive coastal flaw lead network along the landfast ice edge (Barber & Hanesiak, 2004; Galley et al., 2012, 2008). Throughout the observational record there has been a significant negative trend in summer sea ice area within the Beaufort Sea as a result of enhanced summer melt (Babb et al., 2019; Hutchings & Rigor, 2012), which has transitioned

the Beaufort Sea from a predominantly MYI cover to a predominantly FYI cover (Galley et al., 2016; Maslanik et al., 2011). This transition has amplified since the mid-2000s (Galley et al., 2016) but can be traced back to a rapid shift towards a younger ice regime during winter 1998 that conditioned the region for its first notable summer minimum (Hutchings & Rigor, 2012; Maslanik et al., 1999). Overall, the younger and thinner ice cover of the Beaufort Sea has become increasingly mobile (e.g. Babb et al., 2019; Petty, et al., 2016) whereas historically the ice cover would lock up under internal stress and be relatively quiescent during winter (Babb et al., 2019). The ice cover of winter 2017 was particularly conditioned to be mobile after the region had been ice-free during September 2016 for the second time in five years (Babb et al., 2019).

The occurrence of an ice-free Beaufort Sea during September 2016 was the result of preconditioning towards younger, thinner ice through enhanced ice export during the prior winter that created an anomalously thin ice cover that broke up early and melted rapidly (Babb et al., 2019). Over the following winter of 2017, a large amount of seasonal ice formed locally in the Beaufort Sea. Here we combine in situ and remotely sensed observations to examine how the prolonged Beaufort Gyre reversal during winter 2017 converged and deformed this seasonal ice cover. We then consider the question: do contrasting mechanisms of winter preconditioning – i.e. ice import, convergence, and dynamic thickening in 2017 compared to export, divergence, and thin ice in 2016 – have any effect on the subsequent summer melt period? Similar to 2013, did the convergent conditions of 2017 reduce summer melt and facilitate a recovery of the Beaufort Sea ice pack? We finally discuss how more frequent reversals of the Beaufort Gyre will impact the ice cover of the Western Arctic in coming decades.

2. Methods:

2.1 Sea Ice Concentration, Drift, Flux, and Age

Daily fields of sea ice concentration and ice drift from 1979 to 2017 were retrieved from the National Snow and Ice Data Center (NSIDC). Specifically, the Sea Ice Concentrations from Nimbus-7 SMMR and DMSP SSIM/I-SSMIS Passive Microwave Data (Version 1 - Cavalieri et al., 1996; updated 2019), which uses the NASA team algorithm to extract sea ice concentration at a spatial resolution of 25 km^2, were used. In terms of ice drift, the Polar Pathfinder Daily 25 km EASE-Grid Sea Ice Motion Vectors (Version 4 – Tschudi et al., 2019) were used. Ice concentration fields were used to calculate the daily regional ice concentration of the Beaufort Sea with regional bounds along 150°W and 75°N

(black lines Figure 1A). Ice drift and concentration were then used to quantify the daily ice flux (F_i – $km^2\ d^{-1}$) at 5 km intervals (i) along the western (150°W) and northern (75°N) gates of the Beaufort Sea (Figure 1) for each day from 1979 to 2017 from the following equation,

$$F_i = \Sigma\ c_i\ u_i\ \Delta x \quad (1)$$

where, c_i is the daily sea ice concentration interpolated to each point, u_i is the daily ice velocity component normal to the gate (zonal velocity at the west gate, meridional velocity at the north gate) interpolated to each point, and Δx is the distance between points along each gate (5 km). Ice flux through the 10 southern-most points of the western gate were excluded from the analysis due to the nearest ice drift vectors being flagged for land contamination. As shown in Babb et al., (2019), this reduced the daily western ice flux by an average value of 105 km^2 and reduced the cumulative monthly ice fluxes by up to 5%, meaning that ice fluxes across the western gate are likely conservative. The sum of F_i along each gate is referred to as the western and northern flux, while the sum of these two fluxes is presented as the net ice transport. Ice fluxes are presented at daily intervals, and as monthly sums and cumulative sums from the day of regional ice breakup (regional sea ice concentration <95%; following Babb et al., 2019) to mid-September. Positive fluxes represent ice import into the Beaufort Sea, whereas negative fluxes represent ice export from the Beaufort Sea. A net import of sea ice is used to infer convergence of the regional ice cover, while net ice export infers divergence of the regional ice cover. Following Kwok and Rothrock (1999), Babb et al., (2019) determined that based on ice drift errors of the Polar Pathfinder dataset from Sumata et al., (2014) (December to April: σ_e = 0.873 km/day; May to October: σ_e = 1.123 km/day), the uncertainty in ice flux across the northern gate is 52 km^2/day during winter and 67 km^2/day during summer, and 41 km^2/day during winter and 56 km^2/day during summer across the western gate. Lastly, ice transport from the Amundsen Gulf into the Beaufort Sea is not considered, as the Polar Pathfinder dataset does not resolve ice drift between Cape Bathurst and Banks Island. Therefore, regional estimates of ice melt are conservative because additional sea ice is typically flushed out of Amundsen Gulf into the Beaufort Sea early in the melt season (Kwok, 2006).

Gridded pan-Arctic estimates of sea ice age were also retrieved from the NSIDC and used to explore the broader impact of the reversal on the distribution of MYI in the Arctic Ocean. The EASE-Grid Sea Ice Age dataset (Version 4 – Tschudi et al., 2019) uses the Polar Pathfinder ice motion dataset described above to track lagrangian parcels of sea ice at weekly steps, ageing parcels by one year if sea ice concentration within their corresponding

grid cell (12.5 km^2) remains above 15% throughout the melt season. If sea ice concentration in a grid cell falls below 15%, those parcels are assumed to have melted.

2.2 Atmospheric reanalysis

Monthly means of Sea Level Pressure (SLP) and 2-m air temperature were retrieved from the ERA-5 reanalysis (Copernicus Climate Change Service (C3S), 2017). Seasonal air temperature anomalies for 2013, 2016 and 2017 were calculated relative to the 1979-2008 climatology.

2.3 Canadian Ice Service Ice Charts

Weekly ice charts from the Canadian Ice Service (CIS) were used to quantify the regional ice concentration by ice type during the 2016-2017 sea ice season and provide historic context. Ice charts primarily use Radarsat-2 imagery to delineate different ice regimes with polygons that present the total concentration and partial concentration (tenths) of up to three different stages of development according to the World Meteorological Organizations egg code. The landfast ice edge is denoted in the weekly ice charts and distinguishes mobile pack ice (maximum total concentration of 9+ -tenths) from landfast ice (total concentration of 10-tenths). Further details on the processing of the ice charts and their applicability are discussed in Galley et al., (2016) and Tivy et al., (2011).

2.4 Sea Ice Thickness, Roughness and Volume:

2.4.1 CryoSat-2 and SMOS

Sea ice freeboard and surface roughness (σ) observations were obtained from the ESA CryoSat-2 satellite, using the Lognormal Altimeter Retracker Model (LARM) algorithm described in Landy et al. (2020). The LARM algorithm is based on simulations of the CryoSat-2 waveform performed with a physical model for the SAR altimeter echo backscattered from sea ice (Landy et al., 2019). The physical echo model accounts for realistic variations in the radar backscattering properties and sea ice surface roughness, at the scale of the CryoSat-2 footprint. Modelled echoes are fit to observed ESA Baseline-C Level 1b CryoSat-2 waveforms with a nonlinear least-squares optimization scheme, solving for the surface elevation, roughness, radar scattering efficiency, and waveform amplitude. The sea ice freeboard is estimated from the elevation difference between ice floes and sea surface height interpolated between leads. Sea ice freeboard distributions obtained with LARM compare closely to those obtained from coincident airborne data from NASAs Operation IceBridge (Landy et al., 2020).

Radar freeboard and surface roughness observations from LARM are sampled onto a 25-km EASE-Grid 2 at monthly intervals for October-April 2010-2019. The radar freeboards are converted to sea ice freeboards, then to estimates for the ice thickness using snow depth and density fields from SnowModel-LG (Liston et al., 2020; J. Stroeve et al., 2020). SnowModel-LG is a spatially distributed Lagrangian snow-evolution modeling system that includes modules for the snow energy budget and snow redistribution into drifts (Liston et al., 2020). It has been applied to estimate snow depth on sea ice, with atmospheric reanalysis forcing fields from ERA5 and MERRA2 (J. Stroeve et al., 2020) and *Polar Pathfinder* ice motion vectors (Tschudi et al., 2019). Sea ice freeboards are obtained from the radar freeboards with a snow-depth dependent correction for the delayed radar wave propagation through snow (Landy et al., 2020). Sea ice thickness is derived from the buoyancy equation, accounting for different densities of FYI and MYI (Alexandrov et al., 2010). In regions where the gridded ice thickness is less than 1 meter, we calculate the weighted mean ice thickness from CryoSat-2 estimates and monthly SMOS thin sea ice thickness (https://icdc.cen.uni-hamburg.de/1/daten/cryosphere/l3c-smos-sit.html) (Tian-Kunze et al., 2014), with the weights provided by respective data uncertainties (e.g. Ricker et al., 2017). A comparison between the sea ice thicknesses derived from CryoSat-2 + SnowModel-LG + SMOS and mean sea ice drafts from the Beaufort Gyre Exploration Program Upward Looking Sonars (ULS) are shown in Supplementary Figure 1. Sea ice volume within each pixel is calculated for each month based on the derived ice thickness and sea ice concentration from the OSI SAF Global Sea Ice Concentration (OSI-401-b) dataset (Eastwood, 2012). Surface roughness represents the root-mean square height of macro-scale surface topography within the CryoSat-2 footprint, assuming a lognormal surface height distribution. Additionally, the fraction of MYI within ice covered grid cells is provided by the OSI SAF ice type product (Eastwood, 2012) and used to classify grid cells as either FYI or MYI types.

We then use the CryoSat-2 surface roughness (σ) observations as a guide to estimate the dynamic versus thermodynamic components of the winter sea ice growth rate. An increase in ice thickness (h) without the surface roughening indicates thermodynamic growth, whereas an increase in thickness with roughening indicates dynamic thickening through pressure ridge formation. The 95th percentile monthly increase in roughness $d\sigma/dt$, from the entire 2011-2018 CryoSat-2 record, is assumed to represent fully dynamic thickening. Gridded $d\sigma/dt$ values are then scaled between zero and this maximum value

and multiplied by the monthly ice thickness increases dh/dt to obtain an estimate for the dynamic component of ice growth (dh_D). The thermodynamic component of ice growth (dh_{TD}) is estimated from the residual monthly thickness increase after removing the dynamic term. This relatively simple analysis will not perfectly determine the exact split between dynamic and thermodynamic terms; however, their relative differences across the record provide a useful guide for understanding seasonal/interannual variations in forcing.

2.4.2 Upward Looking Sonar Ice Draft

In situ observations of ice draft were acquired from Mooring D (74°N, -140°W; red star Figure 1A) of the Beaufort Gyre Exploration Project (BGEP) mooring array which has been deployed in the Canada Basin since summer 2006 and turned over annually (Krishfield & Proshutinsky, 2006; Krishfield et al., 2014). The mooring is equipped with an Upward Looking Sonar (ULS) moored between 20 and 85 m beneath the sea surface and uses a 420 kHz beam to measure the distance to either the sea surface or the underside of sea ice (see *Krishfield et al.,* (2014) for the processing technique). At a nominal depth of 50 m the footprint is estimated to be 2 m in diameter. The ULS samples every 2 s, and after being corrected for tilt and changes in the seawater temperature and salinity, which affect the speed of sound, the estimated accuracy of each range measurement is better than ±0.1 m (Melling & Riedel, 1995). Data were provided in daily frequency counts (10 cm bins) and used to calculate monthly ice draft distributions.

2.4.3 Airborne Ice Thickness Surveys

Airborne ice thickness surveys were conducted over the Beaufort Sea on April 2 and 4, 2017 as part of the PAMARCMIP 2017 airborne campaign. The surveys provide *in situ* observations of total ice thickness (ice plus snow) immediately following the 2017 reversal. During an airborne survey an Electromagnetic Bird (EM Bird) is towed below a fixed wing aircraft at an approximate height of 20 m above the ice surface. A laser altimeter measures the EM Bird's altitude above the snow while the distance to the ice-ocean interface is derived from the measured amplitude and phase of a secondary EM field that is induced in the conductive seawater by a primary field transmitted by the EM Bird (Haas et al., 2010, 2009). Similar to the ULS, the accuracy over level ice is ±0.1 m (Haas et al., 2009), however the thickness of ridged ice is underestimated because the diameter of the EM footprint is 3.7 times the instruments altitude (Reid et al., 2006) and is therefore greater than the width of ridges. Haas and Jochmann (2003) estimate that the thickness of unconsolidated ridges can be underestimated by up to 50%, which leads to an underestimation of ice thickness along

the right tail of ice thickness distributions and an overall conservative estimate of regional sea ice thickness.

2.4.4 Operation IceBridge – Surface Roughness

NASA's Operation IceBridge conducted airborne surveys over the Beaufort Sea during March and April from 2009 to 2019. During these surveys a canonically scanning laser altimeter known as the Airborne Topographic Mapper (ATM) collected high-resolution elevation measurements over the snow covered sea ice with a vertical accuracy of 6.6 cm (Martin et al., 2012; Petty, et al., 2016). Surface roughness was derived as the root mean square of elevation data in 30 m segments along the flight track and distributed as a Level 2 product through the NSIDC (Data Set ID: ILATM2; Studinger, 2014). The ATM instrument is known to suffer from an azimuth-angle dependent basis (Yi et al., 2015), therefore we only consider data along the nadir track to compare roughness measurements from different years. It is important to note that the ATM measures the roughness of snow on sea ice; however, we assume that snow and ice roughness are correlated (Landy et al., 2020).

3. Results:

3.1: Regional sea ice transport and formation

We examine monthly fields of SLP, ice drift and MYI area in the Western Arctic from November 2016 to April 2017 and provide added context of the daily ice fluxes and historical comparison of monthly fluxes across the Beaufort's northern and western gates (Figure 1). Typical anticyclonic ice motion occurred during November and December 2016 leading to the characteristic import of ice into the Beaufort from the north and export of ice westward into the Chukchi Sea (Figure 1). Northern import was nearly three and a half times higher during November 2016 (89,000 km^2) than the 30-year climatology (26,400 km^2) because of the highly mobile, new ice cover that had formed following ice-free conditions only two months prior at the end of summer 2016 (Figure 2). However, because the MYI edge had retreated north of the Beaufort during summer 2016, northern import during November and December was mainly comprised of new ice and resulted in only a narrow tongue of MYI extending into the Beaufort by January. During January, the Beaufort High collapsed leading to a period of pronounced ice import in the first half of January that was nearly offset by ice export during the second half of January (Figure 1B). This opposing pattern resulted in a reduced monthly mean field of ice motion and a net ice flux of near 0

km^2 across both the northern and western gates. North of the Beaufort, there was pronounced northeastward ice drift, advecting MYI towards and northeastwards along the CAA. Without a Beaufort High, anomalous ice motion began during February 2017, and while unusual southeastward ice drift increased northern import by more than 4x the 30-year climatology (2017: 51,000 km^2; climatology: 12,000 km^2) it primarily imported seasonal ice from beyond the band of MYI located along the CAA. In March, instead of the typical SLP gradient between the Beaufort High and Aleutian Low driving westward ice motion in the Beaufort Sea, the SLP gradient had flipped and drove eastward ice motion. This led to anomalously high western import of seasonal ice from the Chukchi Sea into the Beaufort Sea (2017: 32,500 km^2; climatology: -23,500 km^2) and limited the ice flux across the northern gate to essentially zero. Eastward ice motion compacted MYI throughout the western Arctic up against the CAA (Figure 1A). With continental North America to the south, Banks Island to the east and both M'Clure Strait and Amundsen Gulf already containing sea ice, the anomalous import of 87,000 km^2 of sea ice during February and March compared to the 1979-2008 climatological export of -26,000 km^2, caused persistent anomalous convergence within the regional ice cover. Unlike the period of ice export that offset the first pronounced period of ice import during January, the two pronounced periods of ice import in early-February and early-March were followed by limited ice transport that maintained a compact ice cover (Figure 1B).

Subsequently, the Beaufort High returned during April, driving anticyclonic ice motion throughout the western Arctic (Figure 1). Northern import was confined to the eastern Beaufort and aligned with the band of MYI along the CAA, while pronounced westward ice drift through the southern Beaufort Sea drove extremely high western ice export (2017: -107,000 km^2; climatology: -37,000 km^2) during April (Figure 1C). However, note that western ice export during April 2017 remained considerably lower than the pronounced flushing events observed in March 2013 (-192,000 km^2) and February and April 2016 (-182,000 and -187,000 km^2, respectively; outliers noted by crosses in Figure 1C).

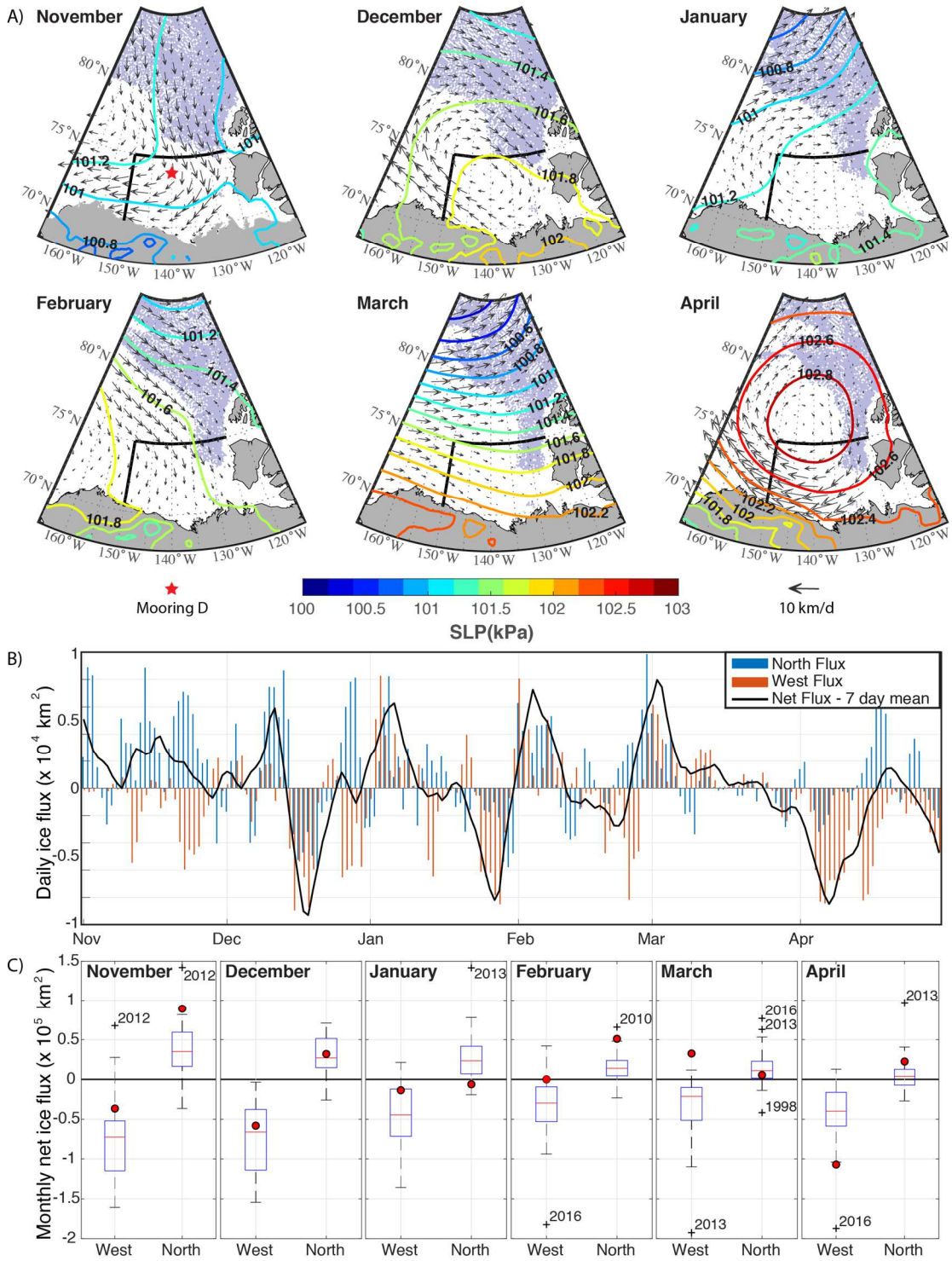

Figure 1: A) Monthly maps of SLP (lines), ice drift (vector) and MYI areas (blue shading; NSIDC Ice Age dataset) for November 2016 to April 2017. Note a red star denotes the location of Mooring D. B) Daily ice flux across the western and northern gates with the 7-day running mean of net ice flux from November 2016 to April 2017. C) Monthly box plots of ice flux across the western and northern gates for the 1979-2016 climatology with the median flux denoted by the red line, blue box denoting the

interquartiles and whiskers extending to 2.7σ. Outliers are denoted by black crosses. Fluxes from 2016-2017 are denoted by red circles.

Ice motion within the Beaufort Gyre and the associated import/export of sea ice through the Beaufort Sea dictates the seasonal evolution of the regional ice cover and how the ice cover is conditioned for the following melt season. The evolution of the regional ice cover from ice-free conditions in September 2016 through to summer 2017 is presented in Figure 2. In September 2016 the region was ice-free, leaving a vast area for new sea ice to begin forming in early-October. By mid-November a complete ice cover had formed and was primarily comprised of seasonal ice types that progressed from new ice in October and November to thin, medium and thick FYI types throughout winter (Figure 2a). A small percentage of new ice was present during December and January within the Cape Bathurst polynya flaw lead complex, but declined in coverage as the reversal began in February and was notably absent from the region during March (Figure 2a).

By the end of March 2017, 97% of the Beaufort ice cover was medium and thick FYI, as MYI was not replenished within the Beaufort Sea during winter 2016-2017. Historically the regional MYI concentration has gradually increased following the loss of MYI during summer (Figure 2B). Even after the first occurrence of an ice-free Beaufort Sea in 2012, the regional MYI concentration increased through winter 2012-2013 to concentrations during spring and summer 2013 that were typical of the region since 1998 (Figure 2B). However, this did not occur through winter 2016-2017. Instead, the northward retreat of the MYI edge during summer 2016 limited MYI import under anticyclonic ice motion during November and December 2016. From January to mid-April the regional MYI concentration remained around 3% (Figure 2A) as a result of the reversal limiting northern import to approximately 0 km^2 during January and March, and importing seasonal ice from the northeast as opposed to MYI from along the CAA during February (Figure 1).

In April 2017, the return of the Beaufort High and anticyclonic ice drift slowly increased the regional MYI concentration while also bringing about the return of new ice within leads in the divergent ice pack and the coastal flaw leads (Figure 2A). New ice formation maintained a complete ice cover until May when the ice cover broke-up, but new ice disappeared quickly during May and early-June as the regional ice cover declined. During July, there was a slight increase in the regional ice cover that was facilitated by an increase in MYI coverage (Figure 2B). From an annual peak of 12% in early August, MYI concentration slightly declined during August and September, but the loss of FYI was much

greater and ultimately by mid-September 2017 the total regional ice concentration fell to 15%, the fourth lowest of the satellite record (Figure 2C). From 1984 to 2017 there was a significant ($p < 0.05$) negative trend of -11.2%/decade in September sea ice concentration within the Beaufort Sea that was capped off by the four lowest concentrations within the record occurring between 2012 and 2017.

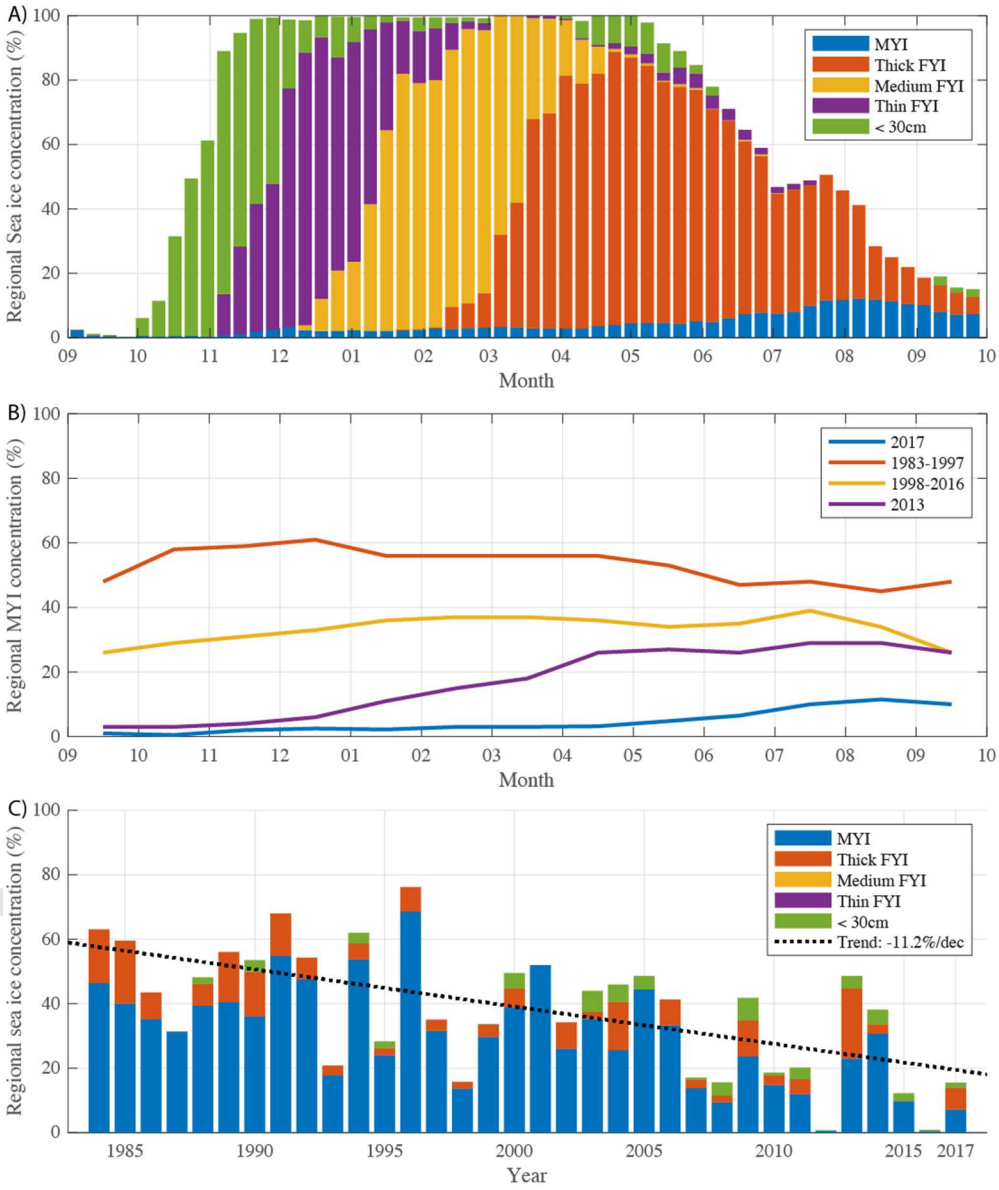

Figure 2: A) Seasonal evolution of the Beaufort ice cover (< 75°N; 150°W – 120°W) by ice type from September 2016 to October 2017. B) Monthly mean MYI concentration during the 2016-2017 ice season, 2012-2013 ice season, and the 1983-1997 and 1998-2016 means. C) 1984-2017 time series of regional sea ice area by ice type during mid-September, with the annual trend.

3.2 Regional sea ice thickness and roughness

Beyond tracking the types of ice present within the Beaufort, monthly remotely sensed fields of ice thickness and roughness provide a three-dimensional view of the evolution of the ice cover from November 2016 to April 2017 (Figure 3; Table 1). During November the absence of MYI and prevalence of new and thin FYI lead to a fairly homogenous and relatively smooth (regional mean roughness: $\bar{\sigma}$ = 0.05 m) ice cover throughout the Beaufort with a regional mean thickness ($\overline{h_i}$) of 0.54 m and negative ice thickness anomalies throughout the northern portion of the region that is typically covered by MYI (Figure 3). The ice cover grew thicker through December ($\overline{h_i}$ = 0.95 m) with negative ice thickness anomalies throughout the region except for a small area of positive ice thickness anomalies in the northeast where MYI had been imported. This area of positive ice thickness anomalies expanded throughout the eastern Beaufort during January as sea ice converged against the CAA in the first half of the month, causing sea ice roughness to increase and flipping the regional mean ice thickness anomaly from -0.09 m in December to +0.20 m in January (Table 1). Anomalous ice import and convergence in February spread positive ice thickness anomalies throughout the Beaufort and further amplified the formation of a rougher ice cover. Continued ice import through March drove further convergence that grew the ice cover to an annual peak thickness of 2.01 m, which is 0.41 m greater than the 2011-2018 mean, and created an ice cover that was twice as rough as the 2011-2018 mean with positive ice thickness anomalies throughout a majority of the Beaufort. As the Gyre re-established itself during April ice was exported from the Beaufort, causing the ice to divergence and thereby reducing the mean regional ice thickness ($\overline{h_i}$ = 1.83 m) and ice thickness anomalies, though vast areas of rough sea ice remained in the southern and eastern Beaufort (Figure 3).

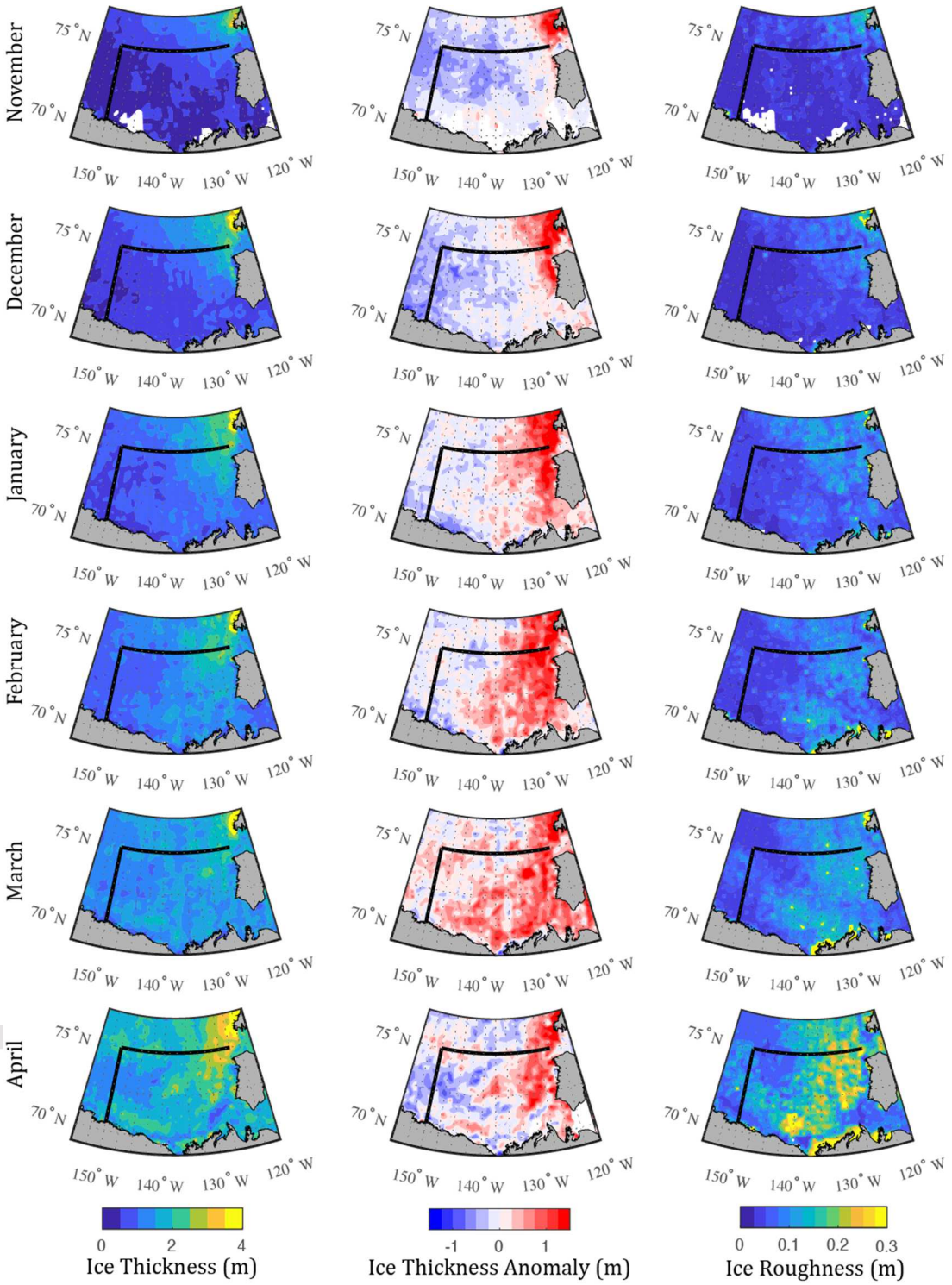

Figure 3: Monthly fields of sea ice thickness (left column), thickness anomalies relative to the 2010-2011 to 2015-2016 mean (middle column) and roughness (right column) in the Beaufort Sea from November 2016 to April 2017.

Table 1: Monthly regional mean ice thickness (h_i), and roughness ($\bar{\sigma}$) from November 2016 to April 2017, with the monthly means from the Cryosat-2 record and associated anomalies ($\Delta\bar{h}_i$ and $\Delta\bar{\sigma}$) during winter 2016-2017.

	$\bar{h}_i$ (m)	$\bar{h}_{i\,clim}$	$\Delta\bar{h}_i$	$\bar{\sigma}$	$\bar{\sigma}_{clim}$	$\Delta\bar{\sigma}$
November	0.54	0.72	-0.18 (-25%	0.050	0.066	-0.016 (-24%)
December	0.95	1.04	-0.09 (-9%)	0.067	0.075	-0.008 (-11%)
January	1.40	1.20	+0.20 (17%)	0.094	0.070	+0.024 (24%)
February	1.76	1.43	+0.33 (23%)	0.119	0.076	+0.043 (57%)
March	2.01	1.60	+0.41 (26%)	0.157	0.079	+0.078 (99%)
April	1.83	1.71	+0.12 (7%)	0.143	0.084	+0.060 (71%)

Our estimate of the split between dynamic and thermodynamic sea ice growth (Figure 4) indicates that increased ice thickness and roughness during January, February and March 2017 was the result of enhanced dynamic growth (dh_D: 0.20, 0.16 and 0.12 m, respectively) through convergent ice drift. Typically, at this time of year dynamic growth is limited (2011-2018 monthly mean dh_D: 0.05, 0.07 and 0.05 m, respectively) and thermodynamic growth dictates the monthly change in regional ice thickness (Figure 4). Since winter 2010-2011, dynamic ice growth has typically been greatest in November and December, particularly in 2012 and 2016 when a predominantly seasonal ice cover formed following ice-free conditions, and decreased through winter as the thicker ice cover became less mobile. However, dynamic growth persisted throughout winter 2016-2017 and accounted for approximately half of the regional ice growth from October to March (2016-2017 dh_D = 0.96 m, dh = 1.91 m). This is 61% greater than the 2011-2018 mean winter dynamic growth of 0.55 m and, in conjunction with slightly elevated thermodynamic growth (2016-2017 dh_{TD}: 0.95 m; 2011-2018 $\overline{dh}_{TD}$: 0.83m), led to the greatest seasonal ice growth within the Beaufort Sea (1.91 m). Even though the ice cover was anomalously thin in October, and thinned during April, a month when ice growth is highly variable, the regional ice thickness during March was the greatest of the CryoSat-2 record ($\bar{h}_i$ = 2.01 m; Figure 4; Table 1).

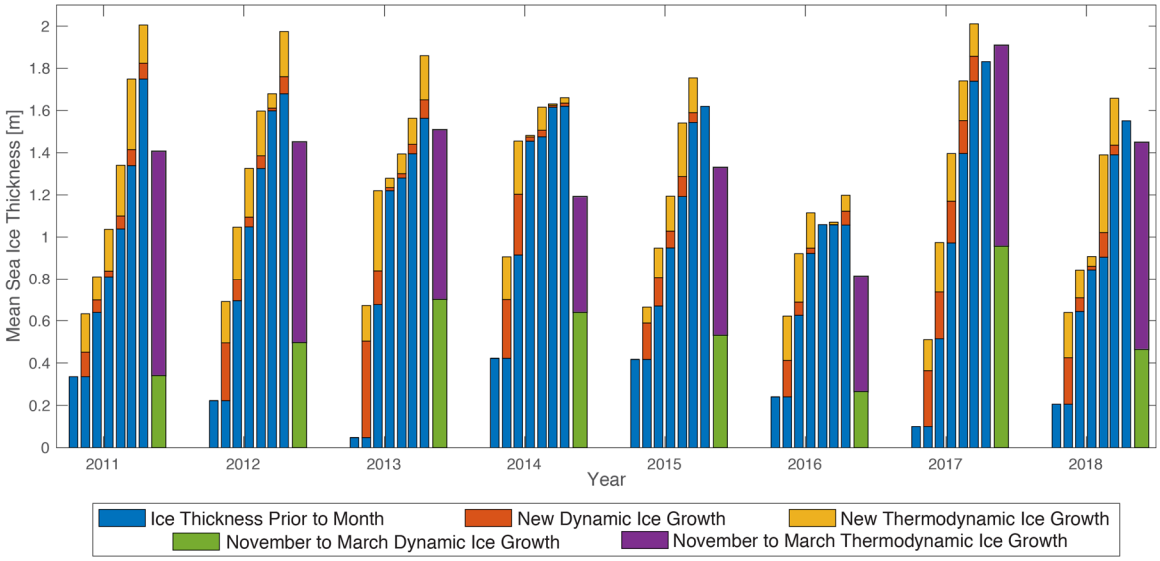

Figure 4: Monthly estimates of the dynamic and thermodynamic contributions to the change in mean regional ice thickness. The November to March sum is presented for each winter.

As a result of enhanced dynamic ice growth during the reversal, by March the regional ice cover was twice as rough as the average in the CryoSat-2 record (2017: $\bar{\sigma}$ = 0.16 m; 2011-2018 mean: $\bar{\sigma}$ = 0.08 m; Figure 5; Table 2). This is in spite of the fact that MYI was confined to a narrow band near Banks Island (note the MYI edge differs slightly between the ice charts in Figure 5 and NSIDC ice age in Figure 1), making for a predominantly seasonal ice cover, which is generally smoother than MYI (Figure 5; Table 2; Petty, et al., 2016). Segmenting the roughness by ice type reveals that FYI during March 2017 was over twice the roughness of FYI during the other 7-years of the CryoSat-2 record and was in fact 50% rougher than average MYI during the others years (Table 2). Ultimately the 2016-2017 regional ice cover evolved from a -25% ice volume anomaly in November 2016 (November 2016: 228 km^3, 2010-2017 mean: 305 km^3) to a +23% anomaly in March 2017 (March 2017: 965 km^3, 2011-2018 mean: 782 km^3) at which time it had the greatest regional sea ice volume within the CryoSat-2 record.

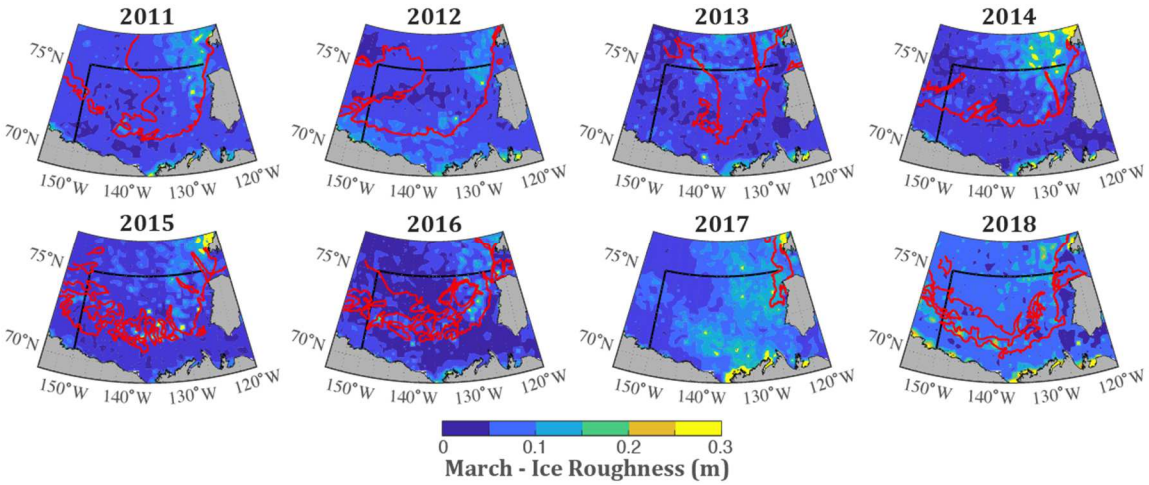

Figure 5: Sea ice roughness during March from 2011-2018 in the Beaufort Sea with the MYI ice edge (5-tenths) from the last ice chart of March overlaid in red. Note that there is some discrepancy between the MYI edge in Figure 1, which is derived from lagrangian tracking of ice parcels, compared to the MYI edge provided in weekly ice charts derived from Radarsat-2.

Table 2: Regional mean ice roughness during March from 2011-2018 and the climatological mean. The last two columns differentiate roughness between FYI and MYI dominated areas within the Beaufort Sea.

	$\overline{\sigma}$	$\overline{\sigma}_{FYI}$	$\overline{\sigma}_{MYI}$
2011	0.077	0.071	0.098
2012	0.085	0.083	0.092
2013	0.074	0.074	0.092
2014	0.083	0.075	0.092
2015	0.090	0.082	0.103
2016	0.065	0.062	0.092
2017	0.157	0.140	0.193
2018	0.079	0.079	0.085
Climatology	0.079	0.075	0.940

3.3 In situ observations of ice thickness and roughness

In situ observations of the Beaufort ice pack provide more detail on the evolution of the ice cover through the 2016-2017 sea ice season and clarify how the reversal affected the ice cover. Observations of ice draft from Mooring D in the northwestern Beaufort Sea (red star - Figure 1A) highlights the monthly evolution of the ice cover from the onset of ice formation in October 2016 through to the end of the ice-covered season in July 2017 (Figure 6A; Table 3). The monthly modal draft increased from thin ice (0.35 m) in October to a peak

in May (1.45 m), before open water became the most frequent observation during June and the modal ice draft declined during July (Figure 6A; Table 3). Monthly modes were below the historic modes throughout the 2016-2017 sea ice season (Table 3), whereas the monthly mean draft was 0.62 m thinner than the historic mean during November, but exceeded the historic mean by 0.05 m during the peak of the reversal in March. The presence of open water and thin ice (drafts < 0.5 m) declined from 83% of the observations in November to 18% during January, 7% during February and down to 2% during March (Table 3), while at the same time, drafts > 2.5 m increased from 0% in November to 4% in January, 6% in February and 18% in March (Figure 6A). Relative to the previous decade of observations at Mooring D, January 2017 was notably thinner than all other years except for 2013, which also followed an ice-free September and features a similarly shallow right tail of the distribution (Figure 6B). While the modal draft remained low relative to previous years during February and March, the presence of deeper drafts along the right tail increased (Figure 6C and 6D). By March the right tail was the greatest of the 11-year record at Mooring D, and only similar to March 2011 (Figure 6D), at which time the MYI concentration at Mooring D was 3-tenths. Compared to the previous ten years of observations, convergence during winter 2017 reduced the presence of thin ice by 75% and increased the presence of deep drafts by 64% during March (Table 3). However, as the ice cover diverged during April 2017 the coverage of open water and thin ice increased to 13% and the presence of deeper drafts along the right tail declined back to the lowest of the 11-year record (Figure 6E). Deeper drafts returned to 12% of observations during May and June (Figure 6A; Table 3) as the anticyclonic gyre advected thicker deformed ice that had formed in the eastern Beaufort during the reversal and remained in the eastern Beaufort (Figure 1) over the mooring months later.

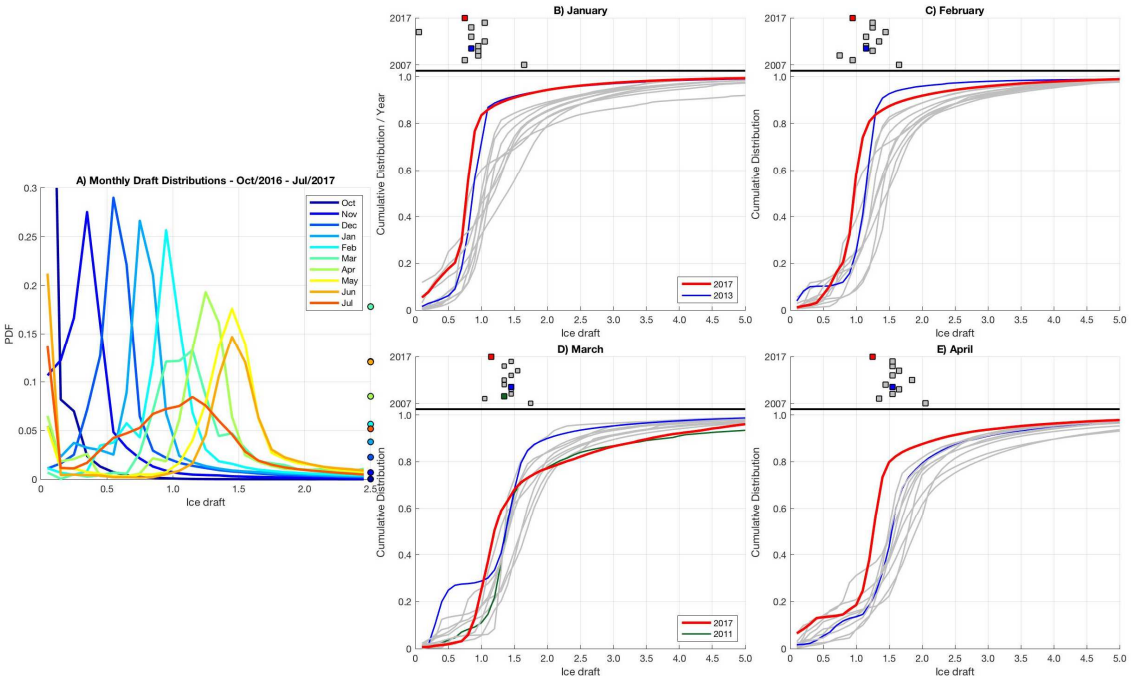

Figure 6: Cumulative ice draft distributions from Mooring D of the BGEP array (location Figure 5). A) Monthly cumulative distributions from September 2016 to August 2017 with the cumulative fraction of observations >= 2.5 m represented by the dot on the right side. B – E) Cumulative distributions for January, February, March and April from 2007 – 2017, with 2017 in red and other years of interest coloured. Squares at the top of the B - E denote monthly modal roughnesses from each year (2007-2017).

Table 3: Monthly modal and mean drafts, and the fraction of drafts < 0.5 m and > 2.5 m at Mooring D from November to June during 2016-2017 and the historical means from 2007-2016. OW indicates Open Water was the modal observation.

		Nov	Dec	Jan	Feb	Mar	Apr	May	Jun
2016-17	Mode	0.35	0.55	0.75	0.95	1.15	1.25	1.45	OW
	Mean	0.40	0.72	0.89	1.15	1.71	1.41	1.72	1.57
	< 0.5 m	83%	25%	18%	7%	2%	13%	9%	23%
	> 2.5 m	1%	2%	4%	6%	18%	9%	12%	12%
Historic mean	Mode	0.55	0.65	0.95	1.25	1.45	1.65	1.65	1.00
	Mean	1.02	1.15	1.36	1.48	1.66	1.89	1.99	1.83
	< 0.5 m	48%	18%	10%	7%	7%	8%	12%	15%
	> 2.5 m	9%	9%	10%	9%	11%	16%	20%	17%

Airborne observations conducted during mid-March 2017 in the midst of the reversal confirm the spatial pattern in surface roughness observed by CryoSat-2 and provide added detail (Figure 7). The ice cover beyond the landfast ice along the west coast of Banks Island and the southern Beaufort Sea, just north of the Mackenzie Delta, was particularly rough (Figure 7A). Typically the coastal flaw lead system leads to a younger, thinner and therefore smoother ice cover in these areas (Melling & Riedel, 1996), however convergent ice drift prevented the flaw lead from opening during the reversal and instead created a deformed ice cover in its place (Figure 7A). Breaking down the aerial observations of surface roughness into four sub-regions, it is clear that roughness distributions from the Western and Central Beaufort, with respective modes of 5 and 6 cm, and means of 9 and 11 cm, were fairly typical of FYI roughness distributions in the Western Arctic (Petty, et al., 2016). Conversely, convergence against the landfast ice in the Eastern and Southern Beaufort created much rougher ice, with respective modes of 6.5 and 9 cm, means of 19 and 16 cm, and approximately 50% of the observations having a surface rougher than 15 cm, compared to only 10% in the Western and Central Beaufort (Figure 7B).

For historic context, the survey route west of Banks Island has been flown four times since 2014, and 2017 was by far the roughest of those four years with a mean approximately twice that of previous years (2017: 20.75 cm; 2014: 6.95 cm; 2015: 12.45 cm; 2018: 11.80 cm) and a much broader distribution compared to pronounced unimodal distributions over smooth surfaces during other years (Figure 7C). This route covers a dynamic area that is close to the flaw lead that forms between the landfast ice edge along western Banks Island and the eastern edge of the MYI tongue that enters the Beaufort (Figure 5). During winter 2016-2017 MYI was confined to the northeastern Beaufort Sea, with MYI concentrations >= 5-tenths present in a narrow band compressed against the northwestern coast of Banks Island. The 2017 survey off the west coast of Banks Island crossed this area of 5-tenths MYI, which may have contributed to the patch of rough ice offshore of northwestern Banks Island. However, the patch of rough ice offshore of southwestern Banks Island was solely FYI that had been deformed during the reversal. Overall, observations of surface roughness from Operation IceBridge flights in mid-March 2017 confirm that convergent ice drift against the landfast ice cover of the Southern and Eastern Beaufort during the 2017 reversal created an ice cover that was anomalously rough, particularly for FYI.

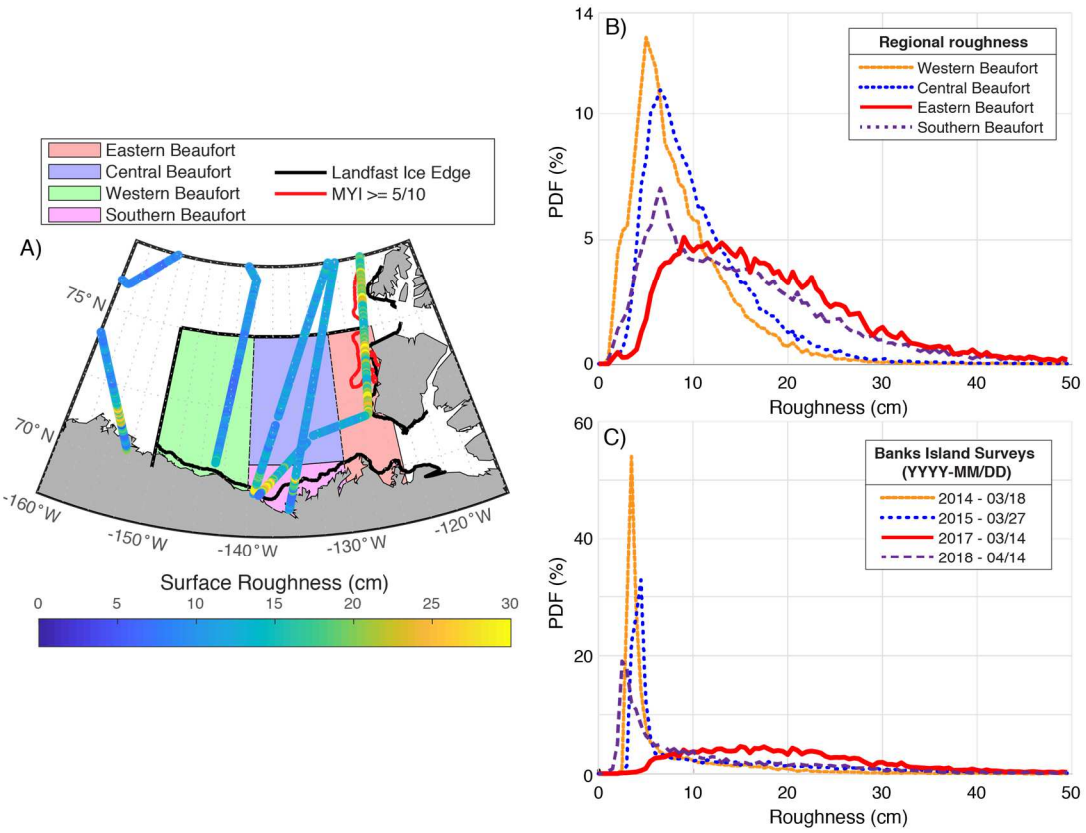

Figure 7: A) Ice Roughness from Operation IceBridge surveys over the Beaufort Sea during mid-March, 2017. The Beaufort region has been divided into 4-sub regions; Western, Central, Eastern and Southern. The MYI edge (red line) and landfast ice edge (black line) from the March 13, 2017 ice chart are presented. B) PDFs of ice roughness in the four sub-regions. C) PDFs of the four OIB surveys conducted west of the landfast ice off the west coast of Banks Island during 2014, 2015, 2017 and 2018 with survey dates presented as mm/dd.

The heavily deformed ice cover that existed following the reversal was fortuitously sampled for total ice thickness during two airborne surveys on April 2 and 4, 2017. The two surveys occurred while the ice cover remained quiescent after the reversal and before the return of pronounced anticyclonic ice drift in April. Starting from the edge of the landfast ice cover, the two surveys collectively reveal a unimodal ice thickness distribution with a mode of 1.45 m and an overall mean of 2.16 m (Figure 8D). Although the mooring and airborne surveys did not overlap, they show general agreement with modal drafts of 1.25 m and 1.35 m during March and April (Figure 7) corresponding to approximately 90% of the modal total ice thickness. The mean airborne ice thickness of 2.16 m is 0.15 and 0.33 m greater than the regional monthly mean ice thickness of 2.01 and 1.83 m during March and April, respectively, though the airborne surveys were focused in the southeastern Beaufort where deformation was greatest. Past ice thickness distributions from aerial surveys over the

Beaufort Sea have typically revealed a multimodal distribution with modes that reflect open water and new ice (< 0.5 m), FYI (1.7 to 2.3 m) and MYI (3.0+ m) (Haas et al., 2010). Similar to the mooring observations, aerial surveys reveal very little thin ice (< 0.5 m) and a trailing right tail that, given there was no MYI along the survey routes (Figure 8A), reflect FYI deformed during the reversal. Cumulative ice thickness distributions from the three sections of the zonal portion of the eastern survey (A, B and C in Figure 8A) show that the three distributions were similar up to 1.5 m, but that the presence of thicker ice increased towards Banks Island, with observations of ice thicker than 2 m increasing from 25% in section A to 40% in section C (Figure 8B). Given that deformed FYI is known to be under-sampled by the EM Bird, these observations provide a conservative estimate of the presence and thickness of deformed FYI in the Beaufort Sea following the 2017 reversal.

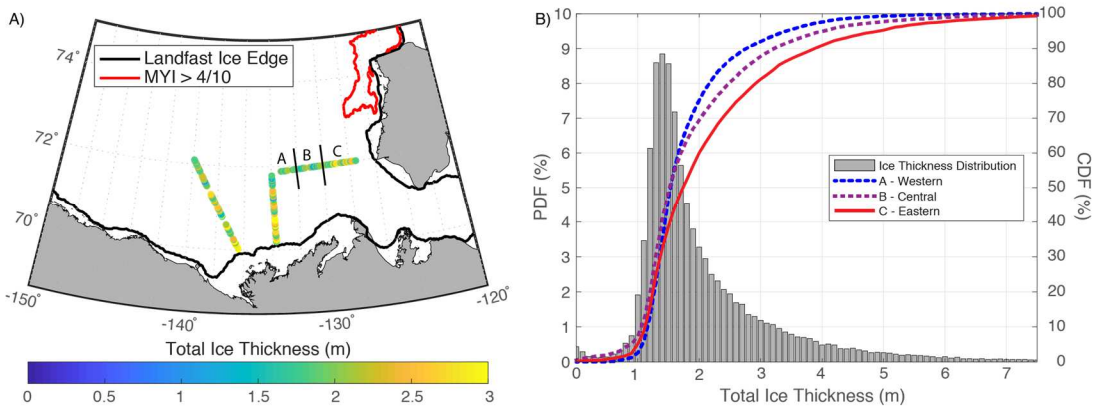

Figure 8: A) Airborne surveys of total ice thickness from April 2 and 4, 2017 with the MYI edge (red line) and landfast ice edge (black line) from the April 3 ice chart presented. B) Ice thickness distribution (PDF) from the two surveys (blue bars) and the cumulative ice thickness distribution (CDF) of the three sections (A, B and C) from the zonal transect towards Banks Island on April 2.

The fact that the modal total ice thickness was between 0.4 and 0.7 m below historic FYI modes and that the monthly modal draft from March 2017 was 0.3 m thinner than the modal draft from the prior decade indicates that the seasonal ice cover of winter 2017 was inherently thin and would have made for an anomalously thin ice cover by the end of winter 2017. However, dynamic thickening as a result of convergent ice drift during the 2017 reversal limited the presence of thin ice, redistributed seasonal ice into thicker ridges and rubble fields and made for an overall thicker and rougher ice cover with the greatest end of winter ice volume over the CryoSat-2 record. This seemingly prepared the 2017 ice cover to

be more resilient to summer melt with the potential to limit regional ice loss during summer.

3.4 Sea ice breakup and melt following the reversal

Following the 2017 reversal, the Beaufort High re-established itself during April, restoring anticyclonic circulation (Figure 1). In spite of concurrent western and northern export during early-April and overall anomalously high western export during April (Figure 1), a complete ice cover was maintained through new ice formation (Figure 2) until the regional ice cover broke up on May 7, 2017 (vertical dashed line Figure 9). This was one week earlier than the long-term regional mean (black line Figure 9A), and at a similar time to years of previous sea ice minima (1998, 2008 and 2012; Figure 9A). The regional sea ice area declined quickly during May and June, and while northern import caused sea ice area to plateau during July (seen as a slight increase in the ice charts in Figure 2), eventually the ice cover fell to its fourth lowest September sea ice area since observations began in 1984 and was near previous minima of 1998 and 2008 (Figure 9A; Figure 2). During the melt season from breakup on May 7 to mid-September the net ice export was -54,500 km^2, which means that 380,600 km^2 of sea ice melted locally during this time (Figure 9C). This is the second highest ice area to melt within the Beaufort during summer over the 40-year satellite record, after only 2016, and is 26% greater than the 1998 – 2016 mean of 301,050 km^2 (Babb et al., 2019). However, in contrast to the ice cover of 2016, which was conditioned towards a younger, thinner ice cover by the end of winter, the ice cover at the end of winter 2017 was predominantly thick, deformed ice and therefore conditioned to withstand summer melt. Furthermore, September sea ice area during 2017 was similar to the minima of 1998 and 2008, both of which were preconditioned towards thinner ice during the prior winter (Hutchings & Perovich, 2015; Maslanik et al., 1999; Perovich et al., 2011). Ice melt in the Beaufort during summer 2017 was apparently large enough to leave the region ice-free once again, but northern import during June and July (Figure 9B) advected MYI into the Beaufort (Figure 2), halting regional ice loss (Figure 9A) and forming a MYI tongue that persisted through summer in the Eastern Beaufort Sea (ice chart – not shown). Ultimately, conditioning towards a thick, deformed seasonal ice cover during the winter 2017 reversal did not limit summer ice loss.

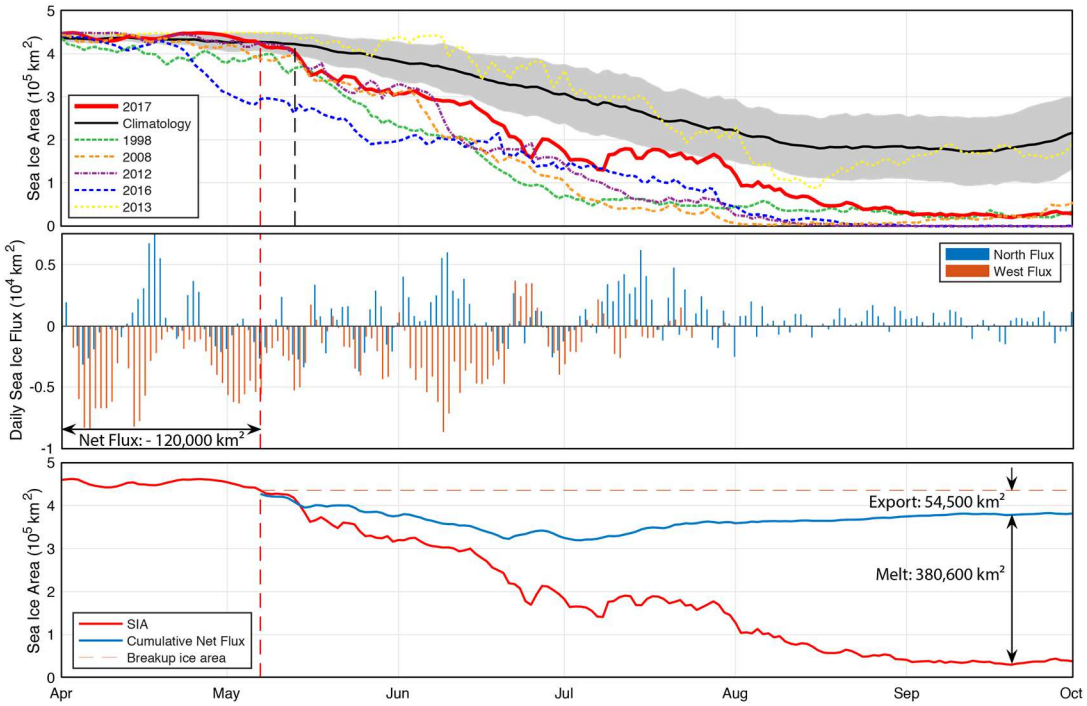

Figure 9: The seasonal time series from April to September of (a) daily regional sea ice area (km²) for 2017, the four years of regional sea ice minima, 2013 and the 1979 climatology ± 1 standard deviation (grey shading). (b) Daily net ice flux (km²) across the north (blue) and west (red) flux gates. (c) Daily sea ice area during 2017 and the daily cumulative ice transport from the day of regional breakup (regional sea ice concentration < 95%, 7 May – vertical dashed red line). The vertical dashed black line in a) denotes the climatological date of breakup. The horizontal dashed line in c) denotes the regional sea ice area on the day of breakup and is used to determine the net cumulative ice flux between breakup and mid-September that in turn estimates the area of ice lost to regional melt.

4. Discussion:

4.1: Connecting winter dynamics to summer thermodynamics.

Recent work in Babb et al., (2019) showed that enhanced ice export and divergence within the Beaufort Sea during winter 2016 preconditioned the region towards thinner ice types that promoted earlier breakup and rapid ice loss during summer. Conversely the 2017 reversal caused anomalous ice import and substantial dynamic thickening through convergence during winter, creating an ice cover that during March 2017 was nearly 1 m thicker than the ice cover of March 2016 (Figure 4). In comparison to spring 2016, the icescape at the start of April 2017 should therefore have been much more resilient to summer melt. However, ice melted rapidly during both summers and while the Beaufort

was ice-free during September 2016, only a tongue of MYI persisted through summer 2017 as the Beaufort fell to its fourth lowest regional sea ice concentration.

The idea that a reversal of the Beaufort Gyre during winter may condition the region for reduced summer ice melt is based on the recovery of the Beaufort ice cover during September 2013 following a short reversal of the gyre in April 2013 (Figure 2C). Similar to the 2017 reversal, the 2013 reversal increased regional ice thickness through convergent eastward ice drift (Figure 4). Interestingly the April 2013 reversal followed a pronounced export event during March 2013 (Figure 1C; Beitsch et al., 2014) that, similar to winter 2016, conditioned the Beaufort towards younger thinner ice types (Figure 6D) and therefore a thinner regional ice cover (Figure 4; Babb et al., 2019). However, the reversal of April 2013 countered this earlier conditioning and instead of a thin ice cover entering the melt season, created a thick, deformed, and consolidated ice cover (Figure 6E) that delayed breakup (Figure 9A) and limited summer ice melt (Figure 2C; Babb et al., 2019). The fact that a thin end-of-winter ice cover in 2016 completely melted during summer, contrasted by the recovery of summer sea ice following a late-winter reversal in 2013 provokes the idea that reversals of the Beaufort Gyre during winter reduce summer ice loss in the Beaufort Sea. Yet, this was not the case following the prolonged 2017 reversal.

With the return of the Beaufort Gyre in April 2017 the ice cover of the Beaufort Sea was significantly altered from a consolidated, deformed ice pack in late-March/early-April when the airborne surveys were flown, to a fractured divergent ice cover. The presence of new and thin ice types increased from 1-2% in March to >10% in April and early May (Figure 2), as new ice formation offset ice export and maintained a complete ice cover until May 7 when the ice cover broke up (Figure 9). From April 1 to May 7, 140,000 km^2 of the deformed ice cover was exported westward into the Chukchi Sea and only 20,000 km^2 was imported from the north for a net export of 120,000 km^2 (Figure 1; Figure 9B). This means that approximately 25% of the ice cover that had undergone the reversal had been exported out of the region and replaced by primarily new ice and open water. The remaining 75% of the deformed ice diverged, reducing internal stress within the ice pack, thereby facilitating the relaxation or disintegration of ridges formed during the reversal. This process of ridge disintegration has been observed in previous studies of dynamic ice regimes in the Central Arctic Ocean and Fram Strait (e.g. Davis & Wadhams, 1995; Hansen et al., 2013; Steer et al., 2008) and is known to occur more easily in seasonal ice ridges that are less consolidated than ridges in older ice floes (Hansen et al., 2013). The apparent disintegration of ridged

seasonal ice in 2017 is evident in ice draft distributions at Mooring D, where the right tail of the distribution dropped from an 11-year high in March to an 11-year low during April (Figure 6). Without such a strong presence of heavily deformed ice along the right tail of the ice draft distribution, the Beaufort ice cover returned to its relatively thin state that was evident from thin modal ice drafts throughout winter 2016-2017 (Figure 6) and a thin modal total ice thickness (Figure 8). Additionally there was a considerable drop in regional ice thickness during April 2017 (Figure 4). Following the reversal of April 2013, the deep draft tail of the distribution did not rapidly drop or 'relax' in this way (Figure 6) and mean thickness did not decline (Figure 4) because the ice cover remained consolidated. Hence, whilst net ice export following breakup on May 7 only contributed to the loss of 15% of the regional ice cover during summer 2017 (Figure 9C), ice export and divergence during the month prior to breakup undid a majority of the conditioning from the 2017 reversal, opposite to what had occurred in 2013. This dramatically altered the ice cover and once again promoted early breakup and rapid summer ice loss in a similar fashion to 2016.

It is clear from the comparison of 2013, 2016 and 2017 that winter dynamics can condition the ice cover for enhanced melt (e.g. 2016), or that conditioning towards either thinner (e.g. 2013) or thicker (e.g. 2017) ice may be quickly undone by dynamics during early spring. Convergence of the ice pack during the April 2013 reversal negated the conditioning towards younger thinner ice that occurred as a result of divergent drift during March 2013, and delayed breakup. In contrast, divergence of the ice pack during April 2017 negated conditioning towards a deformed ice cover during the 2017 reversal and promoted earlier breakup of the ice cover. Ice dynamics during April within the Beaufort Sea are highly variable. Over the 8-years of the CryoSat-2 record examined here, the regional ice cover grew substantially thicker during three years (2011, 2012 and 2013), it slightly thickened twice (2014 and 2016) and it thinned three times (2015, 2017, 2018). These changes affect the state of the ice cover just prior to the melt season and contribute to the timing of breakup, which is dictated by dynamic forcing (Steele et al., 2015). The timing of breakup exerts a substantial influence on the melt season as it determines when solar heating of the upper ocean can begin to drive the ice albedo feedback loop, which amplifies bottom and lateral melt of the ice cover (Babb et al., 2016; Perovich et al., 2008, 2011). Due to its role in driving sea ice melt, the beginning of the ice-albedo feedback creates a barrier to accurate seasonal sea ice predictions around the Arctic, specifically in the Beaufort (Bonan et al., 2019; Bushuk et al., 2020). Hence, getting a better understanding of how

winter dynamics affect breakup, which in turn affects summer melt, is required to expand the capability of seasonal ice predictions.

Beyond the timing of breakup and the ice-albedo feedback, atmospheric conditions also contribute to the evolution of the ice cover through the melt season by not only affecting surface melt but also dictating how compact the ice cover remains. During summer 2013 a weak SLP gradient over the Beaufort Sea maintained a consolidated ice cover and limited the ice-albedo feedback (Kwok, 2015), while negative air temperature anomalies (Figure 10A) reduced surface melt (Kwok et al., 2018). Conversely, a pronounced SLP gradient over the Beaufort Sea during summers 2016 and 2017 drove westward motion that diverged the ice pack and fostered an accelerated ice albedo feedback, while positive air temperature anomalies (Figure 10) likely increased surface melt and amplified ice loss. Ultimately winter conditioning is only able to carry through the melt season with complimentary summer conditions, if both of these conditions occur, as they did in the Beaufort during 2013, summer ice melt can be limited and the ice cover can recover. But with only one of these factors at play (e.g. 2017) then there may be no recovery and ice loss may only be tempered by summer ice import, specifically the import of MYI.

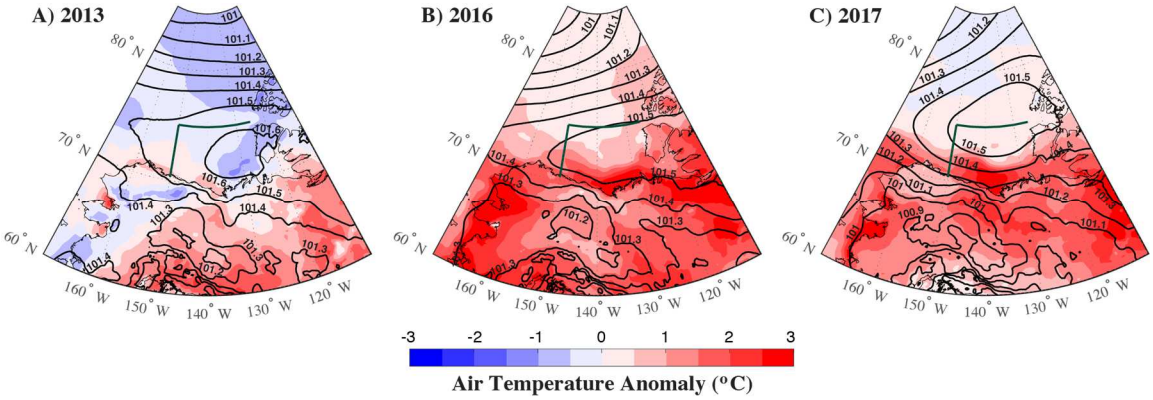

Figure 10: Mean SLP fields and 2 m air temperature anomalies over the Beaufort from May 1 to August 31 in A) 2013, B) 2016 and C) 2017. Anomalies are relative to a 1979-2008 30-year climatology.

The idea that a thick, deformed seasonal ice cover created in winter can essentially be undone with no lasting effect into the melt season has implications for the broader Arctic, which is increasingly covered by seasonal ice types (Kwok et al., 2013) and will likely transition to a complete seasonal ice cover following the projected occurrence of an ice-free summer before 2050 (SIMIP, 2020). The transition towards a seasonal ice cover makes the Arctic ice pack inherently more mobile and dynamic (Kwok et al., 2013; Rampal et al.,

2009), offering the potential for increased dynamic deformation under convergent ice motion that may increase the resiliency of an inherently thinner seasonal ice cover entering the melt season. However, as our study has shown, conditioning towards a dynamically thick seasonal ice cover can quickly be undone through divergent ice drift that fractures the ice cover and allows seasonal ridges to relax or disintegrate. The inherent fact that deformed FYI is less consolidated than MYI floes, which have been deformed over several years and undergone freeze-thaw cycles, makes deformed FYI more likely to disintegrate and therefore less resilient to summer melt. It appears that reduced melt of a seasonal ice cover may only occur with complimentary convergent conditions that deform the ice cover during winter and subsequently maintain a consolidated ice cover through summer.

4.2: The impact of the reversal on the distribution of MYI

One of the principal roles of the Beaufort Gyre is to circulate MYI from the High Arctic through the southern marginal seas of the Western Arctic. Historically, MYI would typically be advected through the Beaufort, Chukchi and East Siberian Seas before either recirculating within the gyre or entering the Transpolar Drift Stream and being advected towards Fram Strait. However, increasing summer ice melt over the past two decades has increased MYI melt in the Beaufort Sea (Babb et al., 2016; Kwok & Cunningham, 2010; J. C. Stroeve et al., 2011) and essentially severed the transport of MYI through the gyre beyond the Beaufort Sea (Maslanik et al., 2011). As a result, the Chukchi and East Siberian Seas have become exclusively seasonal ice zones (Maslanik et al., 2011). However, within the Beaufort, MYI has been replenished every winter via the gyre. Even after years of extreme ice loss like 2012 the regional MYI area has recovered (Figure 2B). That is until 2016-2017 when the regional MYI area remained at an observed minimum throughout the year and made for a predominantly seasonal ice cover in the Beaufort Sea (Figure 2) and throughout the western Arctic (Figure 11A).

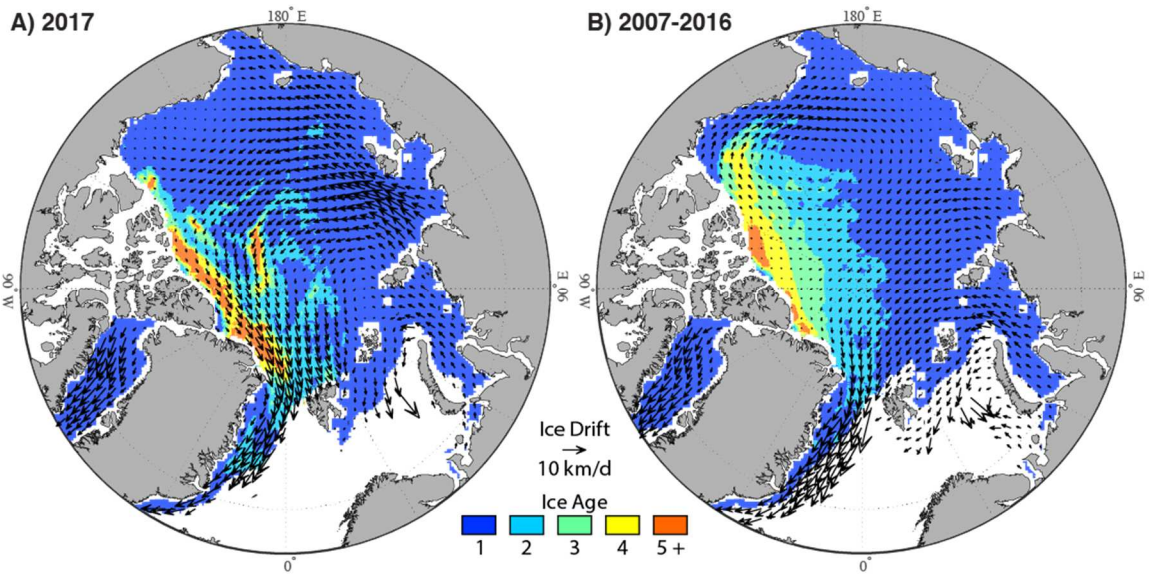

Figure 11: Ice age during the first week of April and the mean field of ice motion from January to March for A) 2017 and b) 2007-2016. Note that in B) ice motion is the mean while ice age is the median. For clarity ice age has been smoothed with a 3x3 sliding mean.

The lack of MYI replenishment within the Beaufort during fall 2016 can be ascribed to the northward retreat of the MYI edge during summer 2016, which limited the availability of MYI to be imported into the Beaufort under typical anticyclonic conditions during November and December 2016 (Figure 1). However, the continued lack of MYI replenishment through winter 2017 was due to the reversal of the Beaufort Gyre, which considerably altered the pan-Arctic pattern of sea ice motion (Figure 11). As opposed to a pronounced anticyclonic pattern of ice motion through the western Arctic, the reversal made for a more pronounced Transpolar Drift Stream that was drawn further into the western Arctic than usual (Figure 11A). This caused sea ice to converge against the southern end of the western flank of the CAA (Banks and Prince Patrick Islands), thereby limiting MYI transport along the CAA into the Beaufort Sea. North of the Beaufort, anomalously high northeastward ice motion along the CAA drove MYI away from the Beaufort Sea towards Fram Strait. Typically, the MYI cover along the CAA is quiescent as the confluence of the Beaufort Gyre and Transpolar Drift Stream converge the ice cover against the CAA, but with this area of convergence dislocated into the Beaufort the MYI cover in this area was much more mobile. By forcing MYI away from the Beaufort Sea the reversal not only halted MYI import during winter, but also limited MYI import through summer 2017 (Figure 2), as only a narrow band of MYI remained upstream of the Beaufort once the gyre

re-established during April (Figure 1; Figure 11). By limiting MYI transport out of the central Arctic into the Beaufort Sea, the 2017 reversal actually offered the potential to limit MYI melt in the western Arctic during summer 2017 and store MYI in the central Arctic. However, by dislocating MYI towards Fram Strait and altering the source region of ice exported through Fram Strait (e.g. Kwok, 2004) the reversal facilitated an increase in MYI export through Fram Strait during March and April 2017 (Ricker et al., 2018) and likely beyond April into summer 2017. MYI export through Fram Strait negated any potential storage of MYI in the central Arctic through summer 2017 as the reversal simply flipped the area of MYI loss from the western Arctic to the East Greenland Sea. Additionally, the loss of MYI through Fram Strait was only slightly offset by the ageing of thick FYI into MYI in the western Arctic (Figure 2), meaning that overall the pan-Arctic coverage of MYI further declined during 2017.

The impact of the 2017 reversal on the distribution of MYI highlights the precarious nature of the remaining MYI in the central Arctic which is becoming increasingly mobile and can either be: i) advected into the Beaufort Sea where a majority, if not all, will now melt during the subsequent summer (Babb et al., 2016, 2019; Kwok & Cunningham, 2010; Maslanik et al., 2011; J. C. Stroeve et al., 2011), ii) exported through Fram Strait into the North Atlantic where it melts (Hansen et al., 2013; Kwok, 2009), iii) exported through the increasingly mobile Nares Strait into Baffin Bay (Kwok et al., 2010; Moore & McNeil, 2018; Ryan & Münchow, 2017) where it may be transported great distances (Barber et al., 2018) but does eventually melt out in the Labrador Sea or Baffin Bay, or iv) exported into the increasingly mobile CAA where it may persist for several years as it gradually migrates through the region (Howell & Brady, 2019; Howell et al., 2013) towards the Northwest Passage (Haas & Howell, 2015).

The loss of MYI in the Arctic Ocean remains one of the key climate-induced changes of the northern polar environment, and due to its location within the Beaufort Gyre the Beaufort Sea is a critical area for MYI. Whereas once the Beaufort acted as the 'safest' haven for MYI exiting the Central Arctic, providing a route for floes to circulate within the ocean for many years, several studies have shown that it is now increasingly unlikely this ice can even last one summer transiting the Beaufort Sea. Additionally, negative trends in summer sea ice area and the occurrence of two ice-free Septembers in recent years has reduced the amount of FYI that persists through summer and is available to 'age' into MYI come fall freeze-up. Within this work we have shown that winter conditioning towards heavily

deformed FYI only slightly increased the amount of FYI that persisted through summer 2017 relative to the last two decades (Figure 2C), and that only under complimentary atmospheric conditions that maintain a compact ice cover and thereby limit the ice albedo feedback, is deformed FYI able to persist through summer (e.g. 2013; Figure 2C) and develop into MYI.

4.3 Reversals in a changing Arctic

Clearly, reversals exert a significant impact on the state of the Arctic ice cover by altering the pan-Arctic fields of sea ice motion which in turn influences where sea ice convergence takes place and the source area of sea ice exported through Fram Strait. The decline in the Arctic ice cover has already expanded the occurrence of reversals from summer to year-round (Asplin et al., 2009; Lukovich & Barber, 2006), and has amplified the magnitude and duration of these reversals (Moore et al., 2018). Furthermore, the decline in the Arctic ice cover has made for a more mobile ice cover that is increasingly responsive to this anomalous atmospheric forcing, and more easily deformed by the convergence that occurs during reversals as ice is advected eastward against the CAA. With sea ice loss projected to persist and even amplify through the 21st century, it has been suggested that reversals may become more common in the coming years (Moore et al., 2018). Which begs the question, how will more frequent and prolonged reversals affect the increasingly seasonal ice cover of the Arctic Ocean?

Several studies have projected a decrease in SLP over the western Arctic (Labe et al., 2018) and an associated weakening of the Beaufort High through the 21st century (Casas-Prat & Wang, 2020), making the Beaufort High more prone to collapse as it did during winter 2017. In particular, the collapse of the Beaufort High during winter 2017 was the result of cyclonic intrusions from the north Atlantic that occurred due to an anomalously thin ice cover in the Barents Sea during Fall 2016 (Moore et al., 2018). Given that ice extent in the Barents Sea has already declined significantly and the area is projected to be ice-free year-round by the mid-21st century (Onarheim & Årthun, 2017), it seems the conditions that facilitated the collapse of the Beaufort High during winter 2017 may occur more frequently and that a weakened Beaufort High will be susceptible to collapse more easily. Furthermore, the continued transition towards a seasonal ice cover in the Beaufort Sea, which is inherently thinner and more mobile, will be more responsive and malleable to these reversals than the thicker MYI cover that historically covered the Arctic Ocean. With a

weaker ice cover enabling stronger feedbacks between ocean, ice and atmosphere, it is more likely the Beaufort High will collapse, as we saw in 2017, under conditions that in an Arctic Ocean dominated by MYI may once have resisted such collapse.

The occurrence of more frequent and prolonged reversals of the Beaufort Gyre would have a considerable impact on the ice mass balance and freshwater content of the Arctic Ocean, which would trickle down to affect various other physical, biological and chemical processes in the Arctic Ocean. In terms of the ice mass balance, reversals promote deformation of the ice cover and limit the presence of biologically active coastal flaw leads in the western Arctic. Conversely, north of the Beaufort Sea, the 2017 reversal displaced MYI out of the central Arctic and increased MYI export through Fram Strait. More frequent reversals in the coming years may allow the remaining MYI to be more easily flushed out of the Arctic, expediting the transition towards a seasonal pan-Arctic ice cover. Although MYI loss through Fram Strait may be partially offset if deformed FYI in the Beaufort is able to persist through summer and age into MYI, which is what happened in 2013 (Figure 2*c*). Beyond the ice cover, reversals facilitate the release of freshwater from the reservoir that accumulates within the gyre under typical anticyclonic circulation (Giles et al., 2012; Manucharyan & Spall, 2016). Freshwater within the gyre is of particular interest because it not only impacts biogeochemical processes in the western Arctic (Carmack et al., 2016), but also presents a potential risk to downstream areas such as regions of deep-water formation in the North Atlantic that could be inundated with freshwater if the gyre were to weaken or reverse (Aagaard & Carmack, 1989; Manucharyan & Spall, 2016). In particular, the Great Salinity Anomaly in the North Atlantic during the late-1960's and early-1970's has been connected to the release of freshwater from the Arctic Ocean (Dickson et al., 1988; Giles et al., 2012). Although the impact of the 2017 reversal on the freshwater balance of the Beaufort Gyre has yet to be examined and was not discussed in a recent inventory of freshwater in the Gyre (Proshutinsky et al., 2019), it, as highlighted by Petty (2018), remains an area for future research.

5. Conclusions:

The collapse of the Beaufort High during winter 2017 caused the typically anticyclonic Beaufort Gyre to undergo its most prolonged reversal within the observational record (since 1978). The reversal altered the pan-Arctic fields of ice motion and thereby impacted sea ice dynamics, MYI transport and ultimately the state of the ice cover prior to

the 2017 melt season. As opposed to the typical anticyclonic pattern of ice motion through the western Arctic, sea ice was advected eastward against the western edge of the CAA, causing ice to converge against Banks Island and limiting MYI import into the Beaufort Sea. Following ice-free conditions during the previous summer, a predominantly seasonal ice cover formed through Fall 2016, creating an anomalously thin (-9%) and smooth (-11%) ice cover. Anomalous eastward ice motion during the reversal increased ice import during February and March, and caused the ice cover to converge against the landfast ice in the Beaufort Sea. Convergent ice drift limited the formation of leads and redistributed areas of thin ice into ridges; it precluded coastal flaw leads from opening and dramatically increased the presence of thicker deformed ice. Ultimately the reversal flipped the ice cover from anomalously thin and smooth conditions in December, to anomalously thick (+26%) and rough (+99%) conditions at the end of March by increasing dynamic ice growth at a time of year when dynamic ice growth is typically subdued. Following the reversal the Beaufort Sea was covered by a consolidated, deformed, thick ice cover that was theoretically conditioned to limit summer melt. However, The Beaufort Gyre returned in April, driving anomalously high western ice export and divergent ice drift in the Beaufort Sea that opened up the ice cover. New ice formed in opening leads, the coastal flaw leads opened and ridges formed during the reversal disintegrated. By the time the regional ice cover broke-up on May 7, 25% of the ice cover that underwent the reversal had been exported and the remaining 75% had diverged, reducing the volume of deformed ice and partially returning the ice cover to its fundamentally thin ice state that existed prior to the reversal. Divergence caused the ice cover to breakup 2-weeks prior to the climatological mean, which initiated the ice albedo feedback, while divergent atmospheric forcing during the melt season amplified the ice albedo feedback. Positive summer air temperature anomalies also amplified ice melt, leading to the second highest regional ice melt of the satellite record and fourth lowest regional September sea ice concentration. Ice melt was strong enough to raise the possibility of another ice-free September in the Beaufort, but MYI import during June and July provided a temporary pause in regional ice loss and formed a MYI tongue that persisted through summer in the eastern Beaufort Sea.

The 2017 reversal of the Beaufort Gyre dynamically consolidated the seasonal ice cover of the Beaufort Sea into the highest end of winter ice volume of the CryoSat-2 record which might reasonably have been expected to limit summer melt. This expectation was based on the recovery of the ice cover in 2013, which followed a short reversal in April that

thickened the ice cover through convergent ice drift. However, following the 2013 reversal, the ice pack remained consolidated and never 'relaxed', whereas during 2017 the pronounced export and divergence during April 2017 significantly altered the ice cover. This delayed breakup during spring 2013 and the onset of the ice albedo feedback, whereas in 2017 ice export facilitated an early breakup and initiated the ice albedo feedback much earlier in the year. Because the 2017 reversal did not facilitate a recovery of the Beaufort ice cover, it emphasizes that summer ice melt can only be limited when convergent conditions during winter are complimented by convergent and stable atmospheric conditions during summer. Our analysis of the Beaufort Sea case studies in 2013, 2016 and 2017 strongly support the theory of Bushuk et al., (2020) that synoptically-driven ice mass convergence and negative ice growth feedbacks limit seasonal predictions of summer ice area. The increasingly seasonal ice cover of the Beaufort is becoming more sensitive to synoptic events, such as the 2017 reversal, that decouple winter preconditioning from summer ice melt. As the Arctic continues to change in response to a declining ice cover reversals are projected to occur more frequently, which will impact the state of the Arctic ice cover and have implications for the resiliency of the ice cover to summer melt.

Acknowledgements:

This work was supported by D.G. Barber's Canada Research Chair. The Natural Sciences and Engineering Research Council of Canada (NSERC) supports D.G Babb through a post-graduate scholarship-doctoral, and both R.J Galley and D.G. Barber through the discovery grant program. D.G. Babb is additionally supported by the Canadian Meteorological and Oceanographic Society (CMOS). J.C. Landy is supported by the ESA Living Planet Fellowship: ESA/4000125582/18/I-NS (Arctic-SummIT) and the Natural Environment Research Council Grants NE/T000546/1 (PRE-MELT) and NE/R012849/1 (Diatom-ARCTIC). This is a contribution to the Arctic Science Partnership (www.asp-net.org). CIS ice charts are freely available online. Sea ice concentration, drift and age datasets are available from the National Snow and Ice Data Center (NASA-Team sea ice concentration - https://nsidc.org/data/NSIDC-0051/versions/1; Polar Pathfinder 25 km Drift v4 - https://nsidc.org/data/nsidc-0116/versions/4; EASE-Grid Sea Ice Age v4 - https://nsidc.org/data/NSIDC-0611/versions/4). The monthly Cryosat-2/SMOS sea ice thickness and roughness dataset is available from https://data.bas.ac.uk/full-record.php?id=GB/NERC/BAS/PDC/01257. Operation IceBridge Surface Roughness data is available from the NSIDC (https://nsidc.org/data/ILATM2/versions/2). ULS Ice Draft data from the Beaufort Gyre Exploration Project is available from the WoodsHole Oceanographic Institute (https://www.whoi.edu/page.do?pid=66559). Airborne total ice thickness survey data is being uploaded to the PANGAEA database (https://www.pangaea.de), but is available from either CH or SH. ERA5 reanalysis products are available from the Climate Data Store through the Copernicus Climate Change Service (https://cds.climate.copernicus.eu/cdsapp#!/home). We would like to specifically thank all of the crews, both airborne and ship based, which support the collection of these extremely useful in situ observations in remote environments. Additional thanks to the Editor and two anonymous reviewers for their helpful feedback.

References:

Aagaard, K., & Carmack, E. C. (1989). The role of sea ice and other fresh water in the Arctic circulation. *Journal of Geophysical Research*, *94*(C10), 14485. https://doi.org/10.1029/JC094iC10p14485

Alexandrov, V., Sandven, S., Wahlin, J., & Johannessen, O. M. (2010). The relation between sea ice thickness and freeboard in the Arctic. *Cryosphere*, *4*(3), 373–380. https://doi.org/10.5194/tc-4-373-2010

Asplin, M. G., Lukovich, J. V., & Barber, D. G. (2009). Atmospheric forcing of the beaufort sea ice gyre: Surface pressure climatology and sea ice motion. *Journal of Geophysical Research: Oceans*, *114*(4), 1–13. https://doi.org/10.1029/2008JC005127

Babb, D. G., Galley, R. J., Barber, D. G., & Rysgaard, S. (2016). Physical processes contributing to an ice free Beaufort Sea during September 2012. *Journal of Geophysical Research: Oceans*, *121*, 267–283. https://doi.org/10.1002/2015JC010756

Babb, D. G., Landy, J. C., Barber, D. G., & Galley, R. J. (2019). Winter Sea Ice Export From the Beaufort Sea as a Preconditioning Mechanism for Enhanced Summer Melt: A Case Study of 2016. *Journal of Geophysical Research: Oceans*, *1998*(6575), 6575–6600. https://doi.org/10.1029/2019JC015053

Barber, D. G., Babb, D. G., Ehn, J. K., Chan, W., Matthes, L., Dalman, L. A., … Gariepy, A. (2018). Increasing Mobility of High Arctic Sea Ice Increases Marine Hazards Off the East Coast of Newfoundland. *Geophysical Research Letters*, *45*(5), 2370–2379. https://doi.org/10.1002/2017GL076587

Barber, D. G., & Hanesiak, J. M. (2004). Meteorological forcing of sea ice concentrations in the southern Beaufort Sea over the period 1979 to 2000. *Journal of Geophysical Research C: Oceans*, *109*(6), 1–16. https://doi.org/10.1029/2003JC002027

Beitsch, A., Kaleschke, L., & Kern, S. (2014). Investigating high-resolution AMSR2 sea ice concentrations during the February 2013 fracture event in the beaufort sea. *Remote Sensing*, *6*(5), 3841–3856. https://doi.org/10.3390/rs6053841

Bonan, D. B., Bushuk, M., & Winton, M. (2019). A Spring Barrier for Regional Predictions of Summer Arctic Sea Ice. *Geophysical Research Letters*, *46*(11), 5937–5947. https://doi.org/10.1029/2019GL082947

Bourke, R. H., & Garret, R. P. (1987). Sea ice thickness distribution in the Arctic Ocean. *Cold Regions Science and Technology*, *13*, 259–280.

Bushuk, M., Winton, M., Bonan, D. B., Blanchard-Wrigglesworth, E., & Delworth, T. L. (2020).

A Mechanism for the Arctic Sea Ice Spring Predictability Barrier. *Geophysical Research Letters*, *47*(13), 1–13. https://doi.org/10.1029/2020GL088335

Carmack, E. C., Yamamoto-Kawai, M., Haine, T. W. N., Bacon, S., Bluhm, B. A., Lique, C., … Williams, W. J. (2016). Freshwater and its role in the Arctic Marine System: Sources, disposition, storage, export, and physical and biogeochemical consequences in the Arctic and global oceans. *Journal of Geophysical Research G: Biogeosciences*, *121*(3), 675–717. https://doi.org/10.1002/2015JG003140

Casas-Prat, M., & Wang, X. L. (2020). Projections of extreme ocean waves in the Arctic and potential implications for coastal inundation and erosion. *Journal of Geophysical Research: Oceans*, *n/a*(n/a), e2019JC015745. https://doi.org/10.1029/2019JC015745

Cavalieri, D. J., Parkinson, C. L., Gloersen, P., & Zwally, H. J. (1996). *Sea Ice Concentrations from Nimbus-7 SMMR and DMSP SSM/I-SSMIS PAssive Microwave Data*. Boulder, Colorado, USA.

Copernicus Climate Change Service (C3S). (2017). *ERA5: Fifth generation of ECMWF atmospheric reanalysis of the global climate*. Copernicus Climate Change Service Climate Data Store.

Curry, R., & Mauritzen, C. (2005). Dilution of the Northern North Atlantic Ocean in Recent Decades. *Science*, *308*(5729), 1772–1774.

Davis, N. R., & Wadhams, P. (1995). A statistical analysis of Arctic pressure ridge morphology. *Journal of Geophysical Research*, *100*(C6). https://doi.org/10.1029/95jc00007

Dickson, R. R., Meincke, J., Malmberg, S. A., & Lee, A. J. (1988). The “Great Salinity Anomaly” in the Northern North Atlantic 1968-1982. *Progress in Oceanography*, *20*(2), 103–151. https://doi.org/10.1016/0079-6611(88)90049-3

Eastwood, S. (2012). *OSI SAF Sea Ice Product Manual*. Norway.

Galley, R. J., Babb, D. G., Ogi, M., Else, B. G. T., Geifus, N. X., Crabeck, O., … Rysgaard, S. (2016). Replacement of multiyear sea ice and changes in the open water season duration in the Beaufort Sea since 2004. *Journal of Geophysical Research: Oceans*, *121*(April), 1–18. https://doi.org/10.1002/2015JC011583.Received

Galley, R. J., Else, B. G. T., Howell, S. E. L., Lukovich, J. V., & Barber, D. G. (2012). Landfast Sea Ice Conditions in the Canadian Arctic: 1983-2009. *Arctic*, *65*(2), 133–144. Retrieved from http://www.jstor.org/stable/41638586%0Ahttp://www.jstor.org/stable/

Galley, R. J., Else, B. G. T., Prinsenberg, S., Babb, D. G., & Barber, D. G. (2013). Sea ice

concentration, extent, age, motion and thickness in regions of proposed offshore oil and gas development near the Mackenzie Delta-Canadian Beaufort Sea. *Arctic*, *66*(1), 105–116.

Galley, R. J., Key, E., Barber, D. G., Hwang, B. J., & Ehn, J. K. (2008). Spatial and temporal variability of sea ice in the southern Beaufort Sea and Amundsen Gulf: 1980-2004. *Journal of Geophysical Research: Oceans*, *113*(5), 1–18. https://doi.org/10.1029/2007JC004553

Giles, K. A., Laxon, S. W., Ridout, A. L., Wingham, D. J., & Bacon, S. (2012). Western Arctic Ocean freshwater storage increased by wind-driven spin-up of the Beaufort Gyre. *Nature Geoscience*, *5*(3), 194–197. https://doi.org/10.1038/ngeo1379

Haas, C., Hendricks, S., Eicken, H., & Herber, A. (2010). Synoptic airborne thickness surveys reveal state of Arctic sea ice cover. *Geophysical Research Letters*, *37*(9), n/a-n/a. https://doi.org/10.1029/2010gl042652

Haas, C., & Howell, S. E. L. (2015). Ice thickness in the Northwest Passage. *Geophysical Research Letters*, *42*(18), 7673–7680. https://doi.org/10.1002/2015GL065704

Haas, C., & Jochmann, P. (2003). Continuous EM and ULS thickness profiling in support of ice force measurements. In S. Loeset, B. Bonnemaire, & M. Bjerkas (Eds.), *Proceedings of the 17th International Conference on Port and Ocean Engineering under Arctic Conditions* (pp. 849–856). Trondheim, Norway: Dep. of Civ. and Transp. Eng. Norw. Univ. of Sc. nad Technol.

Haas, C., Lobach, J., Hendricks, S., Rabenstein, L., & Pfaffling, A. (2009). Helicopter-borne measurements of sea ice thickness, using a small and lightweight, digital EM system. *Journal of Applied Geophysics*, *67*(3), 234–241. https://doi.org/10.1016/j.jappgeo.2008.05.005

Hansen, E., Gerland, S., Granskog, M. A., Pavlova, O., Renner, A. H. H., Haapala, J., … Tschudi, M. A. (2013). Thinning of Arctic sea ice observed in Fram Strait: 1990-2011. *Journal of Geophysical Research: Oceans*, *118*(10), 5202–5221. https://doi.org/10.1002/jgrc.20393

Howell, S. E. L., & Brady, M. (2019). The Dynamic Response of Sea Ice to Warming in the Canadian Arctic Archipelago. *Geophysical Research Letters*, *46*(22), 13119–13125. https://doi.org/10.1029/2019GL085116

Howell, S. E. L., Brady, M., Derksen, C., & Kelly, R. E. J. (2016). Recent changes in sea ice area flux through the Beaufort Sea during the summer. *Journal of Geophysical Research:*

Oceans, *121*, 1–14. https://doi.org/10.1002/2015JC011464

Howell, S. E. L., Wohlleben, T., Dabboor, M., Derksen, C., Komarov, A., & Pizzolato, L. (2013). Recent changes in the exchange of sea ice between the Arctic Ocean and the Canadian Arctic Archipelago. *Journal of Geophysical Research: Oceans*, *118*(7), 3595–3607. https://doi.org/10.1002/jgrc.20265

Hutchings, J. K., & Perovich, D. K. (2015). Preconditioning of the 2007 sea-ice melt in the eastern Beaufort Sea, Arctic Ocean. *Annals of Glaciology*, *56*(69), 94–98. https://doi.org/10.3189/2015AoG69A006

Hutchings, J. K., & Rigor, I. G. (2012). Role of ice dynamics in anomalous ice conditions in the Beaufort Sea during 2006 and 2007. *Journal of Geophysical Research: Oceans*, *117*(5), 1–14. https://doi.org/10.1029/2011JC007182

Krishfield, R. A., & Proshutinsky, A. Y. (2006). *BGOS ULS Data Procedure*. Retrieved from https://www.whoi.edu/page.do?pid=66566

Krishfield, R. A., Proshutinsky, A. Y., Tateyama, K., Williams, W. J., Carmack, E. C., McLaughlin, F. A., & Timmermans, M.-L. (2014). Deterioration of perennial sea ice in the Beaufort Gyre from 2003 to 2012 and its impact on the oceanic freshwater cycle. *Journal of Geophysical Research: Oceans*, *119*. https://doi.org/10.1002/2013JC008999

Kwok, R. (2004). Fram Strait sea ice outflow. *Journal of Geophysical Research*, *109*(C1), C01009. https://doi.org/10.1029/2003JC001785

Kwok, R. (2006). Exchange of sea ice between the Arctic Ocean and the Canadian Arctic Archipelago. *Geophysical Research Letters*, *33*(16), 1–5. https://doi.org/10.1029/2006GL027094

Kwok, R. (2009). Outflow of Arctic Ocean sea ice into the Greenland and Barent Seas: 1979-2007. *Journal of Climate*, *22*(9), 2438–2457. https://doi.org/10.1175/2008JCLI2819.1

Kwok, R. (2015). Sea ice convergance along the Arctic coasts of Greenland and the Canadian Arctic Archipelago: Variability and extremes (1992-2014). *Geophysical Research Letters*, *42*, 1–8. https://doi.org/10.1002/2015GL065462

Kwok, R., & Cunningham, G. F. (2010). Contribution of melt in the Beaufort Sea to the decline in Arctic multiyear sea ice coverage: 1993-2009. *Geophysical Research Letters*, *37*(20), 1–5. https://doi.org/10.1029/2010GL044678

Kwok, R., Cunningham, G. F., & Armitage, T. W. K. (2018). Relationship between specular returns in CryoSat-2 data, surface albedo, and Arctic summer minimum ice extent. *Elementa*, *6*. https://doi.org/10.1525/elementa.311

Kwok, R., Pedersen, L. T., Gudmandsen, P., & Pang, S. S. (2010). Large sea ice outflow into the Nares Strait in 2007. *Geophysical Research Letters*, *37*(3). https://doi.org/10.1029/2009GL041872

Kwok, R., & Rothrock, D. A. (1999). Variability of Fram Strait ice flux and North Atlantic Oscillation. *Journal of Geophysical Research*, *104*(C3), 5177–5189.

Kwok, R., Spreen, G., & Pang, S. (2013). Arctic sea ice circulation and drift speed: Decadal trends and ocean currents. *Journal of Geophysical Research: Oceans*, *118*(5), 2408–2425. https://doi.org/10.1002/jgrc.20191

Labe, Z., Peings, Y., & Magnusdottir, G. (2018). Contributions of Ice Thickness to the Atmospheric Response From Projected Arctic Sea Ice Loss. *Geophysical Research Letters*, *45*(11), 5635–5642. https://doi.org/10.1029/2018GL078158

Landy, J. C., Petty, A. A., Tsamados, M., & Stroeve, J. C. (2020). Sea ice roughness overlooked as a key source of uncertainty in CryoSat-2 ice freeboard retrievals. *Journal of Geophysical Research: Oceans*, 1–18. https://doi.org/10.1029/2019jc015820

Landy, J. C., Tsamados, M., & Scharien, R. K. (2019). A Facet-Based Numerical Model for Simulating SAR Altimeter Echoes from Heterogeneous Sea Ice Surfaces. *IEEE Transactions on Geoscience and Remote Sensing*, *57*(7), 4164–4180. https://doi.org/10.1109/TGRS.2018.2889763

LeDrew, E. F., Johnson, D., & Maslanik, J. A. (1991). An examination of atmospheric mechanisms that may be responsible for the annual reversal of the beaufort sea ice field. *International Journal of Climatology*, *11*(8), 841–859. https://doi.org/10.1002/joc.3370110804

Liston, G. E., Itkin, P., Stroeve, J., Tschudi, M., Stewart, J. S., Pedersen, S. H., … Elder, K. (2020). A Lagrangian Snow-Evolution System for Sea-Ice Applications (SnowModel-LG): Part I—Model Description. *Journal of Geophysical Research: Oceans*, *125*(10). https://doi.org/10.1029/2019JC015913

Lukovich, J. V., & Barber, D. G. (2006). Atmospheric controls on sea ice motion in the southern Beaufort Sea. *Journal of Geophysical Research Atmospheres*, *111*(18), 1–12. https://doi.org/10.1029/2005JD006408

Manucharyan, G. E., & Spall, M. A. (2016). Wind-driven freshwater buildup and release in the Beaufort Gyre constrained by mesoscale eddies. *Geophysical Research Letters*, *43*(1), 273–282. https://doi.org/10.1002/2015GL065957

Martin, C. F., Krabill, W. B., Manizade, S. S., Russell, R. L., Sonntag, J. G., Swift, R. N., & Yungel,

J. K. (2012). Airborne Topographic Mapper Calibration Procedures and Accuracy Assessment. In *NASA, Center for Aerospace Information.* Hanover, MD.

Maslanik, J. A., Serreze, M. C., & Agnew, T. (1999). On the record reduction in 1998 Western Arctic sea-ice cover. *Geophysical Research Letters*, *26*(13), 1905–1908. https://doi.org/10.1029/1999GL900426

Maslanik, J. A., Stroeve, J. C., Fowler, C., & Emery, W. (2011). Distribution and trends in Arctic sea ice age through spring 2011. *Geophysical Research Letters*, *38*(13), 2–7. https://doi.org/10.1029/2011GL047735

Mclaren, A. S., Serreze, M. C., & Barry, R. G. (1987). Seasonal Vaiations of Sea Ice Motion in the Canada Basin and their Implications. *Geophysical Research Letters*, *14*(11), 1123–1126.

Melling, H., & Riedel, D. A. (1995). The underside topography of sea ice over the continental shelf of the Beaufort Sea in the winter of 1990. *Journal of Geophysical Research*, *100*(C7), 13,641-13,653.

Melling, H., & Riedel, D. A. (1996). Development of seasonal pack ice in the Beaufort Sea during the winter of 1991-1992: A view from below. *Journal of Geophysical Research C: Oceans*, *101*(C5), 11975–11991. https://doi.org/10.1029/96JC00284

Melling, H., Riedel, D. A., & Gedalof, Z. (2005). Trends in the draft and extent of seasonal pack ice, Canadian Beaufort Sea. *Geophysical Research Letters*, *32*(24), 1–5. https://doi.org/10.1029/2005GL024483

Meneghello, G., Marshall, J., Timmermans, M. L., & Scott, J. (2018). Observations of seasonal upwelling and downwelling in the Beaufort Sea mediated by sea ice. *Journal of Physical Oceanography*, *48*(4), 795–805. https://doi.org/10.1175/JPO-D-17-0188.1

Moore, G. W. K., & McNeil, K. (2018). The Early Collapse of the 2017 Lincoln Sea Ice Arch in Response to Anomalous Sea Ice and Wind Forcing. *Geophysical Research Letters*, *45*, 8343–8351. https://doi.org/10.1029/2018GL078428

Moore, G. W. K., Schweiger, A., Zhang, J., & Steele, M. (2018). Collapse of the 2017 Winter Beaufort High: A Response to Thinning Sea Ice? *Geophysical Research Letters*, *45*, 1–10. https://doi.org/10.1002/2017GL076446

Onarheim, I. H., & Årthun, M. (2017). Toward an ice-free Barents Sea. *Geophysical Research Letters*, *44*(16), 8387–8395. https://doi.org/10.1002/2017GL074304

Perovich, D. K., Richeter-Menge, J. A., Jones, K. F., & Light, B. (2008). Sunlight, water, and ice: Extreme Arctic sea ice melt during the summer of 2007. *Geophysical Research Letters*,

35(11), 2–5. https://doi.org/10.1029/2008GL034007

Perovich, D. K., Richter-Menge, J. A., Jones, K. F., Light, B., Elder, B. C., Polashenski, C., … Lindsay, R. (2011). Arctic sea-ice melt in 2008 and the role of solar heating. *Annals of Glaciology*, *52*(57 PART 2), 355–359. https://doi.org/10.3189/172756411795931714

Petty, A. A. (2018). A Possible Link Between Winter Arctic Sea Ice Decline and a Collapse of the Beaufort High? *Geophysical Research Letters*, *45*, 2016–2019. https://doi.org/10.1002/2018GL077704

Petty, A. A., Hutchings, J. K., Richter-Menge, J. A., & Tschudi, M. A. (2016). Sea ice circulation around the Beaufort Gyre: The changing role of wind forcing and the sea ice state. *Journal of Geophysical Research: Oceans*, *121*, 1–14. https://doi.org/10.1002/2015JC010903

Petty, A. A., Tsamados, M., Kurtz, N. T., Farrell, S. L., Newman, T., Harbeck, J. P., … Richter-Menge, J. A. (2016). Characterizing Arctic sea ice topography using high-resolution IceBridge data. *The Cryosphere*, *10*, 1161–1179. https://doi.org/doi:10.5194/tc-10-1161-2016

Preller, R. H., & Posey, P. G. (1989). A numerical model simulation of a summer reversal of the Beaufort Gyre. *Geophysical Research Letters*, *16*(1), 69–72. https://doi.org/10.1029/GL016i001p00069

Proshutinsky, A., Krishfield, R., Toole, J. M., Timmermans, M. L., Williams, W., Zimmermann, S., … Zhao, J. (2019). Analysis of the Beaufort Gyre Freshwater Content in 2003–2018. *Journal of Geophysical Research: Oceans*, *124*(12), 9658–9689. https://doi.org/10.1029/2019JC015281

Proshutinsky, Andrey, Krishfield, R., Timmermans, M.-L., Toole, J., Carmack, E., McLaughlin, F., … Shimada, K. (2009). Beaufort Gyre freshwater reservoir: State and variability from observations. *Journal of Geophysical Research*, *114*, C00A10. https://doi.org/10.1029/2008JC005104

Rampal, P., Weiss, J., & Marsan, D. (2009). Positive trend in the mean speed and deformation rate of Arctic sea ice, 1979-2007. *Journal of Geophysical Research: Oceans*, *114*(5), 1–14. https://doi.org/10.1029/2008JC005066

Reid, J. E., Pfaffling, A., & Vrbancich, J. (2006). Airborne Electromagnetic Footprints in 1D Earths. *Geophysics*, *71*, G63–G72. https://doi.org/10.1190/1.2187756

Ricker, R., Girard-ardhuin, F., Krumpen, T., & Lique, C. (2018). *Satellite-derived sea ice export and its impact on Arctic ice mass balance*. 3017–3032.

Ricker, R., Hendricks, S., Kaleschke, L., Tian-Kunze, X., King, J., & Haas, C. (2017). A weekly Arctic sea-ice thickness data record from merged CryoSat-2 and SMOS satellite data. *Cryosphere*, *11*(4), 1607–1623. https://doi.org/10.5194/tc-11-1607-2017

Rigor, I. G., & Wallace, J. M. (2002). Response of sea ice to the Arctic Oscillation. *Applied Physics*, 2648–2663. https://doi.org/10.1175/1520-0442(2002)015<2648:ROSITT>2.0.CO;2

Ryan, P. A., & Münchow, A. (2017). Sea ice draft observations in Nares Strait from 2003 to 2012. *Journal of Geophysical Research: Oceans*, *122*(4), 3057–3080. https://doi.org/10.1002/2016JC011966

Serreze, M. C., & Barrett, A. P. (2011). Characteristics of the Beaufort Sea high. *Journal of Climate*, *24*(1), 159–182. https://doi.org/10.1175/2010JCLI3636.1

Serreze, M. C., Barry, R. G., & Mclaren, A. S. (1989). Seasonal Variations in Sea Ice Motion and Effects on Sea Ice Concentration in the Canada Basin. *Journal of Geophysical Research*, *94*(C8), 10,955-10,970.

SIMIP. (2020). Arctic Sea Ice in CMIP6. *Geophysical Research Letters*, *47*(10). https://doi.org/10.1029/2019gl086749

Steele, M., Dickinson, S., Zhang, J., & Lindsay, R. W. (2015). Seasonal ice loss in the Beaufort Sea: Toward synchrony and prediction. *Journal of Geophysical Research: Oceans*, *120*, 1118–1132. https://doi.org/10.1002/2014JC010247

Steer, A., Worby, A., & Heil, P. (2008). Observed changes in sea-ice floe size distribution during early summer in the western Weddell Sea. *Deep-Sea Research Part II: Topical Studies in Oceanography*, *55*(8–9), 933–942. https://doi.org/10.1016/j.dsr2.2007.12.016

Stroeve, J. C., Maslanik, J. A., Serreze, M. C., Rigor, I. G., Meier, W., & Fowler, C. (2011). Sea ice response to an extreme negative phase of the Arctic Oscillation during winter 2009/2010. *Geophysical Research Letters*, *38*(2), 1–6. https://doi.org/10.1029/2010GL045662

Stroeve, J., Liston, G. E., Buzzard, S., Zhou, L., Mallett, R., Barrett, A., … Stewart, J. S. (2020). A Lagrangian Snow Evolution System for Sea Ice Applications (SnowModel-LG): Part II—Analyses. *Journal of Geophysical Research: Oceans*, *125*(10). https://doi.org/10.1029/2019JC015900

Studinger, M. (2014). *IceBridge ATM L2 Icessn Elevation, Slope and Roughness, Version 2*. https://doi.org/10.5067/CPRXXK3F39RV

Sumata, H., Lavergne, T., Girard-Ardhuin, F., Kimura, N., Tschudi, M. A., Kauker, F., … Gerdes, R. (2014). An intercomparison of Arctic ice drift products to deduce uncertainty estimates. *Journal of Geophysical Research: Oceans*, *119*, 4887–4921. https://doi.org/10.1002/2013JC009724

Tian-Kunze, X., Kaleschke, L., Maaß, N., Mäkynen, M., Serra, N., Drusch, M., & Krumpen, T. (2014). SMOS-derived thin sea ice thickness: Algorithm baseline, product specifications and initial verification. *Cryosphere*, *8*(3), 997–1018. https://doi.org/10.5194/tc-8-997-2014

Tilling, R. L., Ridout, A., Shepherd, A., & Wingham, D. J. (2015). Increased Arctic sea ice volume after anomalously low melting in 2013. *Nature Geoscience*, *8*(August), 643–646. https://doi.org/10.1038/NGEO2489

Tivy, A., Howell, S. E. L., Alt, B., McCourt, S., Chagnon, R., Crocker, G., … Yackel, J. J. (2011). Trends and variability in summer sea ice cover in the Canadian Arctic based on the Canadian Ice Service Digital Archive, 1960-2008 and 1968-2008. *Journal of Geophysical Research: Oceans*, *116*(3). https://doi.org/10.1029/2009JC005855

Tschudi, M. A., Meier, W. N., Stewart, J. S., Fowler, C., & Maslanik, J. A. (2019a). *EASE-Grid Sea Ice Age, Version 4*. https://doi.org/https://doi.org/10.5067/UTAV7490FEPB

Tschudi, M. A., Meier, W. N., Stewart, J. S., Fowler, C., & Maslanik, J. A. (2019b). *Polar Pathfinder Daily 25 km EASE-Grid Sea Ice Motion Vectors, Version 4*. https://doi.org/https://doi.org/10.5067/INAWUWO7QH7B

Yi, D., Harbeck, J. P., Manizade, S. S., Kurtz, N. T., Studinger, M., & Hofton, M. (2015). Arctic Sea Ice Freeboard Retrieval With Waveform Characteristics for NASA's Airborne Topographic Mapper (ATM) and Land, Vegetation, and Ice Sensor (LVIS). *IEEE Transactions on Geoscience and Remote Sensing*, *53*(3), 1403–1410. https://doi.org/10.1109/TGRS.2014.2339737

Zhang, J., & Rothrock, D. A. (2003). Modeling global sea ice with a thickness and enthalpy distribution model in generalized curvilinear coordinates. *Monthly Weather Review*, *131*(5), 845–861. https://doi.org/10.1175/1520-0493(2003)131<0845:MGSIWA>2.0.CO;2